

Customer	: ESRIN	Document Ref	: SST_CCI-WP90-DMI-201
Contract No	: 4000109848/13/I-NB	Issue Date	: 1 July 2019
WP No	: 90	Issue	: 1

Project : SST CCI Phase-II

Title : Passive Microwave SST Production and Impact Assessment

Abstract : This document contains the report for WP90 in Phase-II of the SST_cci project.

Author(s) :

Jacob Høyer

Jacob Høyer, Emy Alerskans
and Pia Nielsen-Englyst, DMI.
Mark Worsfold and Simon
Good, Met Office. Kevin
Pearson and Owen Embury,
University of Reading

Checked by :

Chris Merchant

Chris Merchant
Science Leader, UoR
Hugh Kelliher
Project Manager
Space ConneXions Limited

Accepted by :

Craig Donlon
ESA Technical Officer
ESTEC

Distribution : SST_cci team members
ESA (Craig Donlon)

**EUROPEAN SPACE AGENCY
CONTRACT REPORT**

The work described in this report was done under ESA contract.
Responsibility for the contents resides in the author or organisation
that prepared it.

AMENDMENT RECORD

This document shall be amended by releasing a new edition of the document in its entirety. The Amendment Record Sheet below records the history and issue status of this document.

AMENDMENT RECORD SHEET

ISSUE	DATE	REASON FOR CHANGE
0.1	28/02/2019	First draft for internal review
0.2	23/05/2019	Final draft for ESA review
1	01/07/2019	First issue

Table of contents

LIST OF ACRONYMS	1
EXECUTIVE SUMMARY	2
1. INTRODUCTION.....	3
2. CONSTRUCTION OF A LEVEL 2 CLIMATE DATA RECORD OF SEA SURFACE TEMPERATURE FROM PASSIVE MICROWAVE MEASUREMENTS	4
2.1 Introduction.....	4
2.2 Data.....	5
2.2.1 In situ observations.....	5
2.2.2 AMSR-E data	5
2.2.3 AMSR2 data.....	5
2.2.4 Auxiliary data	6
2.2.5 Matchup database	6
2.3 Algorithm development.....	12
2.3.1 WS retrieval algorithm.....	12
2.3.2 SST retrieval algorithm	13
2.3.3 SST uncertainty retrieval algorithm	14
2.3.4 Improved RFI mask.....	16
2.4 Results	19
2.4.1 Sensitivity.....	24
2.4.2 SST uncertainty	25
2.4.3 Time consistency	26
2.5 Discussion.....	27
2.6 Conclusions.....	29
2.7 References.....	29
3. TECHNICAL CONSIDERATIONS FOR THE PMW RETRIEVAL IMPLEMENTATION	34
4. IMPACT ASSESSMENT OF LEVEL 2 PMW CDR ON LEVEL 4 ANALYSIS	35
4.1 Introduction.....	35
4.2 Results	36
4.3 Summary	43
4.4 Bibliography.....	43
5. CONCLUSIONS AND WAY FORWARD	44

LIST OF ACRONYMS

AMSR2	Advanced Scanning Microwave Radiometer 2
AMSR-E	Advanced Microwave Scanning Radiometer for EOS
CCI	Climate Change Initiative
CCMP	Cross-Calibrated Multi-Platform
CDR	Climate Data Record
CIMR	Copernicus Imaging Microwave Radiometer
CMEMS	Copernicus Marine Environment Monitoring Service
DMI	Danish Meteorological Institute
ESA	European Space Agency
GCOM-W1	Global Change Observation Mission 1st – Water
HPCM	High Priority Candidate Mission
IR	Infrared
ICOADS	International Comprehensive Ocean-Atmosphere DataSet
JAXA	Japan Aerospace Exploration Agency
L2	Level 2
L4	Level 4
NWP	Numerical Weather Prediction
OE	Optimal Estimation
OIA	Observation Influence analysis
OSTIA	The Operational Sea Surface Temperature and Sea Ice Analysis
PMW	Passive Microwave
RFI	Radio Frequency Interference
RSS	Remote Sensing Systems
SST	Sea Surface Temperature
TCLW	Total Cloud Liquid Water
TCWV	Total Column Water Vapour
TMI	TRMM Microwave Imager
TRMM	Tropical Rainfall Measuring Mission
WS	Wind Speed

EXECUTIVE SUMMARY

The work reported in this report describes the development of the Passive Microwave (PMW) SST retrieval algorithms for the AMSR-E and AMSR2 instruments and the generation of climate data records for Level 2 (L2) and Level 4 (L4). Furthermore, the impact on L4 products when ingested in the L4 production system is presented. The SST retrieval algorithm validation and developments have been performed using the Multi Sensor Matchup datasets (MMS).

Retrieval algorithms have been developed within WP90 with the purpose of generating a L2P SST climate data record from the AMSR-E and AMSR2 passive microwave satellite observations for the period 2002-2017. The algorithms include wind speed retrievals and SST retrievals, with corresponding uncertainty retrievals and a new and effective method for detecting and removing RFI contamination. The thorough validation results against independent in situ observations demonstrate that the algorithms developed here generate a consistent climate data record, with very good performance, minimal RFI influence and reliable uncertainty estimates. The validation results thus show an overall bias and standard deviation for quality level 4 and 5 AMSR-E and AMSR2 PMW SSTs against in situ drifters of -0.02 ± 0.46 K and 0.002 ± 0.45 K, respectively. The modelled total uncertainty estimates are 0.45 K and 0.44 K, respectively. Furthermore, a sensitivity of 0.9 for the algorithm ensures retrievals that are able to represent the true variability in the SST.

A positive impact was found when the AMSR-E and AMSR2 L2 SSTs was included in L4 SST production system. Outputs indicated that the PMW data were providing information in regions where IR data were not available. However, impacts were not restricted to those regions, with differences in SST found globally. Statistics from comparisons to independent Argo data suggest a positive impact from the use of the PMW data in the L4 system in most regions of the oceans.

The accurate and consistent SST CDR records presented here have demonstrated that PMW satellite observations are valuable for monitoring the oceans in non precipitating conditions. With the uncertainties in the funding for future microwave satellite missions, it is therefore highly recommended that the passive microwave satellite missions, such as the Copernicus Imaging Microwave Radiometer (CIMR) are part of the future satellite constellation.

The general details on the PMW2.0 data products are listed in Table 1 below.

Table 1: Overview of the ESA CCI PMW2.0 data products delivered in WP 90

Acronym	Description	Data coverage	Spatial resolution	Product grid resolution
AMSRE - L2P	L2P SSTs from AMSR-E in L2P format	1 June 2002 - 4 October 2011	75 x 43 km	10 km
AMSR2 - L2P	L2P SSTs from AMSR-2 in L2P format	2 July 2012 - 26 October 2017	62 x 35 km	10 km
L4 Analysis	L4 Analysis including IR L3U and PMW L2P data	1 June 2002 - 26 October 2017	Effective resolution varies with location	0.05 degree

1. INTRODUCTION

Climate data records of Sea Surface Temperature (SST) have been developed for many years using the Infrared (IR) sensors from (A)ATSR, AVHRRs and MODIS. All the infrared observations are, however limited, by cloud cover and obtain SST for typically 10% to 15% of their swath coverage. The errors in SST between IR sensors typically arise from the same parameters, such as unusual atmospheric humidity and aerosol profiles. Microwave observations of SST are limited only by non-precipitating clouds, coastal/sea-ice boundaries and areas of radio-frequency interference, and offer observational records whose errors are likely independent of those of the IR suite.

However, no Microwave SST climate time series have yet been produced and validated previously in SST CCI. The work reported in this report describes the development of the Passive Microwave (PMW) retrieval algorithms for SST retrieval algorithm development, the generation and validation of a L2 climate data set and the impact on level 4 products when ingested in the L4 production system.

The structure of the report is as follows: The SST retrieval development and validation of the L2 PMW SST product is described in Section 3, which is a copy of a scientific paper to be submitted to Remote Sensing of Environment. Section 4 describes the technical considerations when implementing the PMW retrieval algorithms in the GBCS processing system at University of Reading. The impacts of ingesting the PMW data into the ESA CCI level 4 production system are described in Section 5. Finally, the report concludes in Section 6 with conclusions and recommendations for future satellite missions.

2. CONSTRUCTION OF A LEVEL 2 CLIMATE DATA RECORD OF SEA SURFACE TEMPERATURE FROM PASSIVE MICROWAVE MEASUREMENTS

2.1 Introduction

Global Sea Surface Temperatures (SSTs) are important inputs for Numerical Weather Prediction (NWP) (Brasnett and Colan, 2016), coupled models (Liang et al., 2017), ocean models (Le Traon et al., 2015; Yang et al., 2015), SST analyses (Donlon et al., 2012), oceanographic research (Gentemann et al., 2003), air-sea interaction research (Monzikova et al., 2017; Ning et al., 2018), and of broad use in understanding changes to the marine and ecological environment (Chacko, 2017; Ishizaki, 2014). While infrared satellite SSTs have been available since 1981, the satellite microwave radiometer SST record began in 1997 with the Tropical Rainfall Measuring Mission (TRMM) Microwave Imager (TMI) and then continued (with global data) with the launch of the Advanced Microwave Scanning Radiometer for EOS (AMSR-E) and other follow-on instruments. Infrared SSTs' strengths are in their high spatial resolution (typically 1-4 km at nadir) and very good radiometric fidelity, but retrievals are not possible in the presence of clouds and may be compromised in regions with aerosols or unusual water vapour profiles. Passive microwave (PMW) SSTs are at a lower resolution (approximately 50 km) but can be retrieved in all weather conditions except rain. PMW SST data are not used in the presence of Radio Frequency Interference (RFI) or typically within 1-2 footprints from sea ice or land (where the impact of side-lobe contamination in the vicinity of a typically large thermal contrast becomes a significant source of uncertainty). The PMW SST algorithm is designed to account for water vapour and retrievals are not affected by aerosols. Assuming calibration stability over a mission lifetime, these two important features of PMW SSTs make them especially valuable for long-term climate records.

PMW SST retrieval algorithms have been developed by several groups and differ in their approaches. There are statistical regression algorithms, developed through comparisons between measured brightness temperatures and collocated in situ SSTs (Chang et al., 2015; Shibata, 2006), physically-based regression retrieval algorithms developed through radiative transfer modelling (Meissner and Wentz, 2012), and optimal estimation algorithms developed using an iterative forward-model, environmental data, and in situ observations (Nielsen-Englyst et al., 2018). The statistical and physically-based regression algorithms commonly use a multi-stage regression to account for non-linearities in the brightness temperatures' dependence on retrieved variables. The existing algorithms have typically been derived for one satellite at the time and for a limited time period or with a limited in situ observational database for the tuning and validation.

In this paper we describe a statistical regression-based SST retrieval algorithm, which has been developed within the European Space Agency Climate Change Initiative (ESA-CCI) SST project (Merchant et al., 2014) to generate a PMW SST climate data record (CDR). The retrieval algorithm has been derived consistently for AMSR-E and AMSR2 using a large amount of in situ observations. All SST retrievals are accompanied by an uncertainty value and extensive validation has been performed for both the retrievals and the uncertainty estimates. The approach taken in this paper ensures a consistent and reliable multi-satellite SST CDR based only upon Microwave observation that facilitates the uptake within the many applications of SSTs. The paper is structured first with a description of the satellite, in situ and auxiliary data, as well as the matchup database used for algorithm development and validation, in Section 3.2. Thereafter, the retrieval algorithms are described in Section 3.3. The validation results are presented in Section 3.4. Section 3.5 discusses the results and Section 3.6 contains conclusions and ideas for future work.

2.2 Data

2.2.1 In situ observations

In this study we use in situ measured sea surface temperature observations from the International Comprehensive Ocean-Atmosphere DataSet (ICOADS) version 2.5.1 (Woodruff et al., 2011), and measurements from the Met Office Hadley Centre Ensembles dataset version 4.2.0 (EN4, (Good et al., 2013)). Measurements from drifting buoys are the main source of observations but measurements from Argo free-drifting profiling floats (Argo, 2018; Roemmich et al., 2009) have also been used. The drifting buoys measure the sea surface temperature at a depth of about 20 cm in calm water with an uncertainty of approximately 0.2°C. The drifting buoy sea surface temperatures have been quality checked, as described in Atkinson (2014). The quality flags are provided with the data. For Argo floats, the uppermost temperature measurement has been used, which is measured at a typical depth of about 5 m (Gille, 2008), with an uncertainty of 0.002°C (Abraham et al., 2013; Kennedy, 2014). The quality control of the Argo sea surface temperatures is described in (Good et al., 2013). Sea surface temperatures from drifting buoys and Argo floats have previously been used for algorithm development and validation studies (see e.g. Embury et al., 2012; Høyer et al., 2012; Merchant et al., 2012; Nielsen-Englyst et al., 2018; Udaya Bhaskar et al., 2009).

2.2.2 AMSR-E data

The Advanced Microwave Scanning Radiometer for EOS (AMSR-E) is a twelve-channel, six-frequency microwave radiometer supplied by the Japan Aerospace Exploration Agency (JAXA) for the National Aeronautics and Space Administration's (NASA's) Earth Observation System Aqua platform. It measures brightness temperatures at 6.9, 10.7, 18.7, 23.6, 36.5 and 89.0 GHz at both horizontal and vertical polarization and at an Earth incidence angle of approximately 55 degrees. A 1.6 meter offset parabolic reflector antenna collects the microwave radiation and results in spatial resolutions ranging from approximately 56 km at 6.9 GHz to approximately 5 km at 89.0 GHz. The 89.0 GHz channels are sampled every 5 km, all other channels every 10 km. The dataset used in the present study consists of spatially resampled brightness temperatures at the resolution of the 6.9 GHz channel (Ashcroft and Wentz, 2013) and covers the period June 2002 to October 4, 2011.

2.2.3 AMSR2 data

The Advanced Microwave Scanning Radiometer 2 (AMSR2) is an instrument on JAXA's Global Change Observation Mission 1st – Water (GCOM-W1) platform. GCOM-W1 was launched in May 2012 and began collecting data on July 4, 2012. AMSR2 measures brightness temperatures at 6.9, 7.3, 10.7, 18.7, 23.6, 36.5 and 89.0 GHz at both horizontal and vertical polarization and at an Earth incidence angle of approximately 55 degrees. Note the addition of the 7.3 GHz channels relative to AMSR-E, added for RFI mitigation. AMSR2 uses a 2 meter offset parabolic antenna to obtain a spatial resolution ranging from 4 km at 89.0 GHz to approximately 45 kilometres at 6.9 and 7.3 GHz. The 89.0 GHz channels are sampled every 5 km, all other channels every 10 km. We use the *Dataset of Brightness Temperature Modified Using the Antenna Pattern Matching Technique* (Maeda et al., 2016) which contains similar spatially resampled brightness temperatures to the AMSR-E dataset.

2.2.4 Auxiliary data

Several different datasets have been included in the retrieval and analysis to improve and interpret the retrieved parameters. Information of Total Column Water Vapour (TCWV), Total Cloud Liquid Water (TCLW), surface winds and sea ice concentration has been used from the NWP model ERA-Interim (Dee et al., 2011), which has a spatial resolution of 79 km. An additional surface wind speed dataset was included from the Cross-Calibrated Multi-Platform (CCMP) gridded surface vector winds, which is a product that combines many different satellite and in situ observations (Atlas et al., 2011). The product used here is version 2.0, which has a spatial resolution of 0.25 degrees.

2.2.5 Matchup database

2.2.5.1 ESA CCI Multi-sensor Matchup Dataset

The calibration and validation of the retrieval algorithm have been performed using the Multi-sensor Matchup Datasets (MMDs), which have been developed within the ESA-CCI SST project and contain selected pairs of in situ and satellite observations that are within 20 km and 4 hours from each other. Subregions of 21 by 21 AMSR-E and AMSR2 pixels have been extracted around the central matchup positions and the auxiliary information have been extracted for the central points. Separate MMDs have been created for the AMSR-E and the AMSR2 datasets, but they follow the same specifications in terms of data content and format. For more information on the generation of MMDs, see (Block et al., 2018; Nielsen-Englyst et al., 2018). The AMSR-E MMD includes matchups for the period June 2002-October 2011 and the AMSR2 MMD includes matchups for the period July 2012 – December 2016.

2.2.5.2 Training and validation subsets

The performance of the retrieval algorithm is closely linked to the quality of the satellite observations and auxiliary data used. It is therefore essential to exclude erroneous matchups from the training data. The following paragraphs describe the quality control procedures implemented during algorithm development.

The quality of the input data were considered and matchups with a satellite scan quality or 6-36 GHz channel quality indicating bad data were flagged as erroneous. In addition, matchups with brightness temperatures outside the accepted range (0-320 K) were flagged. For valid oceanographic retrievals, the v-pol brightness temperature should always be larger than the h-pol. Hence, to remove obviously bad observations, data were flagged if the difference between the h-pol and v-pol brightness temperature for the 18-36 GHz channels was negative. This check was only performed for the 18-36 GHz channels since they are the channels for which the atmospheric contribution is largest. Furthermore, to exclude low-quality brightness temperature observations, the spatial standard deviation of the 23 V and H and the 36 V and H brightness temperatures were calculated in the 21 by 21 pixel extract surrounding each pixel. Different approaches were used for AMSR-E and AMSR2 data. For AMSR-E matchups, data were flagged as unusable if the standard deviation of the above-mentioned channels exceeded 55, 35, 25 and 25 K, respectively. Due to differences in the distribution of brightness temperatures, the same limits were not applicable for AMSR2 matchups. Thus, to perform a comparable flagging for AMSR2, the 1% of AMSR2 matchups with the highest standard deviation were considered to be of low quality and flagged accordingly.

The quality of the in situ and auxiliary data was also considered. Matchups with an in situ quality control flag indicating bad data were flagged as erroneous. Moreover, matchups with an in situ or NWP SST less than -2°C or greater than 34°C were excluded. In the same way, matchups with NWP or CCMP wind speeds greater than 20 m s^{-1} were also flagged. Together, the above-mentioned checks on the satellite, in situ and auxiliary data constitute quality control checks (denoted “Quality control checks” in Table 1) which ensure that the input data are of sufficient quality.

Further checks are necessary as both atmospheric and surface effects can contaminate the signal and lead to erroneous retrievals. Sea ice and land affect the retrieval due to antenna side-lobe contamination. The satellite land/ocean flag and NWP sea ice fraction was used to flag matchups. If any land or sea ice was detected within the 21×21 pixel extract surrounding each pixel, the matchup was flagged. Diurnal warming effects were accounted for by flagging daytime AMSR-E matchups with wind speeds less than 4 m s^{-1} . For AMSR2, the wind speed limit was increased to 6 m s^{-1} since diurnal warming effects were not completely removed when using the lower limit of 4 m s^{-1} . Furthermore, precipitating clouds compromise the PMW retrievals and these effects must therefore be excluded. To account for contamination due to rain, data were flagged if the 18 GHz v-pol brightness temperature exceeded 240 K. Sun glitter contamination was accounted for by flagging data with a sun glint angle of less than 25 degrees. To avoid contamination due to RFI, two different approaches were used. For AMSR-E, ground-based and space-based RFI was masked out using Table 2 in (Gentemann and Hilburn, 2015) together with observation location and geostationary reflection longitude and latitude, respectively. AMSR2 has an additional channel at 7.3 GHz, which is specifically designed for detection of RFI. Both the 6.9 GHz and 7.3 GHz channels on AMSR2 suffer from RFI contamination, however, the geographical distributions are different, making it possible to use the two channels for RFI detection. Based on this, the absolute difference between the 6.9 and 7.3 GHz channels (both polarizations) was used to mask out RFI if the difference $> 3\text{ K}$. However, the latter of these methods does not completely mask out all RFI and a large signal could still be seen around Ascension Island. To be sure to mask out all RFI-contaminated data, all matchups in the area around Ascension Island (24°W to 6°W longitude and 18°S to 2°S latitude) were masked out for the AMSR2 matchups. Additional steps to further remove RFI-contaminated data will be introduced in Section 3.3.4. As a last quality control, obviously erroneous in situ SSTs were excluded using a $3\text{-}\sigma$ filter on the NWP and in situ SST difference.

Finally, to obtain a more latitudinally representative dataset, the number of matchups per degree of latitude was restricted. Individual limits were imposed for the different years due to the widely varying number of matchups amongst years. In addition, a limit on the number of matchups per year was imposed. Since each year consists of very different numbers of matchups, a limit of 1 million matchups per year was imposed to get a more temporally representative dataset. However, if the number of filtered matchups was less than 700,000 for a year, the even-out-data-by-year restriction was set to 70% of the total number of good matchups to ensure that data from years with fewer matchups are represented in all subsets (see Figure 1). The summary statistics for the different filtering processes are listed in Table 2.

Table 2: The number of matchups after filtering and the percentage of matchups the filtering step removes. The statistics are shown for both the AMSR-E and AMSR2 datasets.

¹ the percentage of matchups removed is relative to all MMD matchups (No filter).

² the percentage of matchups removed is relative to the number of matchups which passed the "Quality control checks" step.

³ the percentage of matchups removed is relative to the number of matchups that passed the "All above checks" step.

Filter	AMSR-E		AMSR2	
	N	% removed	N	% removed
<i>No filter</i>	40,480,306	-	27,796,093	-
<i>Quality control checks</i> ¹	34,340,715	15.2	25,658,424	7.7
<i>Rain</i> ²	34,088,030	0.7	25,114,008	2.1
<i>Sun glint</i> ²	32,269,911	6.0	24,286,797	5.3
<i>RFI</i> ²	31,832,433	7.3	25,295,077	1.4
<i>Land</i> ²	31,285,364	8.9	22,790,471	11.2
<i>Sea ice</i> ²	30,852,455	10.2	22,627,223	11.8
<i>Diurnal warming</i> ²	30,034,321	12.5	18,975,850	26.0
All above checks ¹	22,319,646	44.9	14,821,726	47.5
<i>3-σ filter on NWP and in situ SST diff.</i> ³	21,972,506	1.6	14,588,260	1.6
All checks ¹	21,972,506	45.7	14,588,260	47.5
<i>Even-out-by-latitude</i> ¹	16,322,299	22.9	9,880,565	32.3
<i>Even-out-by-year</i> ¹	8,460,292	50.0	4,918,012	50.2
Total ¹	8,460,292	79.1	4,918,012	82.3

To obtain an independent validation, the MMDs are divided into 7 subsets each (see Figure 1);

- WS1_TRAIN: training subset for step 1 of the wind speed retrieval algorithm;
- WS1_TEST: validation subset for step 1 of the wind speed retrieval algorithm;
- WS2_TRAIN: training subset for step 2 of the wind speed retrieval algorithm;
- WS2_TEST/SST_TRAIN: validation subset for step 2 of the wind speed retrieval algorithm, also used as training subset for the SST retrieval algorithm;
- SST_TEST: validation subset for the SST retrieval algorithm;
- UNCERT_TRAIN: training subset for the SST uncertainty retrieval algorithm; and
- UNCERT_TEST: validation subset for the SST uncertainty retrieval algorithm.

Figure 1 shows the filtering procedures and subsequent subset division of the AMSR-E and AMSR2 MMDs. The “Filtered MMD”-box represents the filtered MMDs where erroneous data have been excluded and the subsets have been made latitudinally and temporally representative. As shown in Figure 1, the filtered MMD is then divided into two subsets, WS1_TRAIN and WS1_TEST, through random selection of matchups. One sixth of the filtered MMD matchups are used for WS1_TRAIN and the rest for WS1_TEST. Following this, the WS1_TEST subset is divided into two subsets; WS2_TRAIN (1/4 of WS1_TEST) and WS2_TEST/SST_TRAIN (3/4 of WS1_TEST), also through random selection of matchups. The fifth subset, SST_TEST, is constructed from the matchups removed by the application of the evening-out filters on the good data. Imposing a restriction on the number of matchups per degree of latitude for these data gives us the SST_TEST subset, which is used as a validation subset for the retrieved SSTs. The total number of matchups in the AMSR-E and AMSR2 SST_TEST subsets is 9,916,606 and 6,279,359, respectively. Finally, the SST_TEST subset is divided, through random selection of matchups, into two subsets for training and validation of the SST uncertainty retrieval; UNCERT_TRAIN (9/10 of SST_TEST) and UNCERT_TEST (1/10 of SST_TEST).

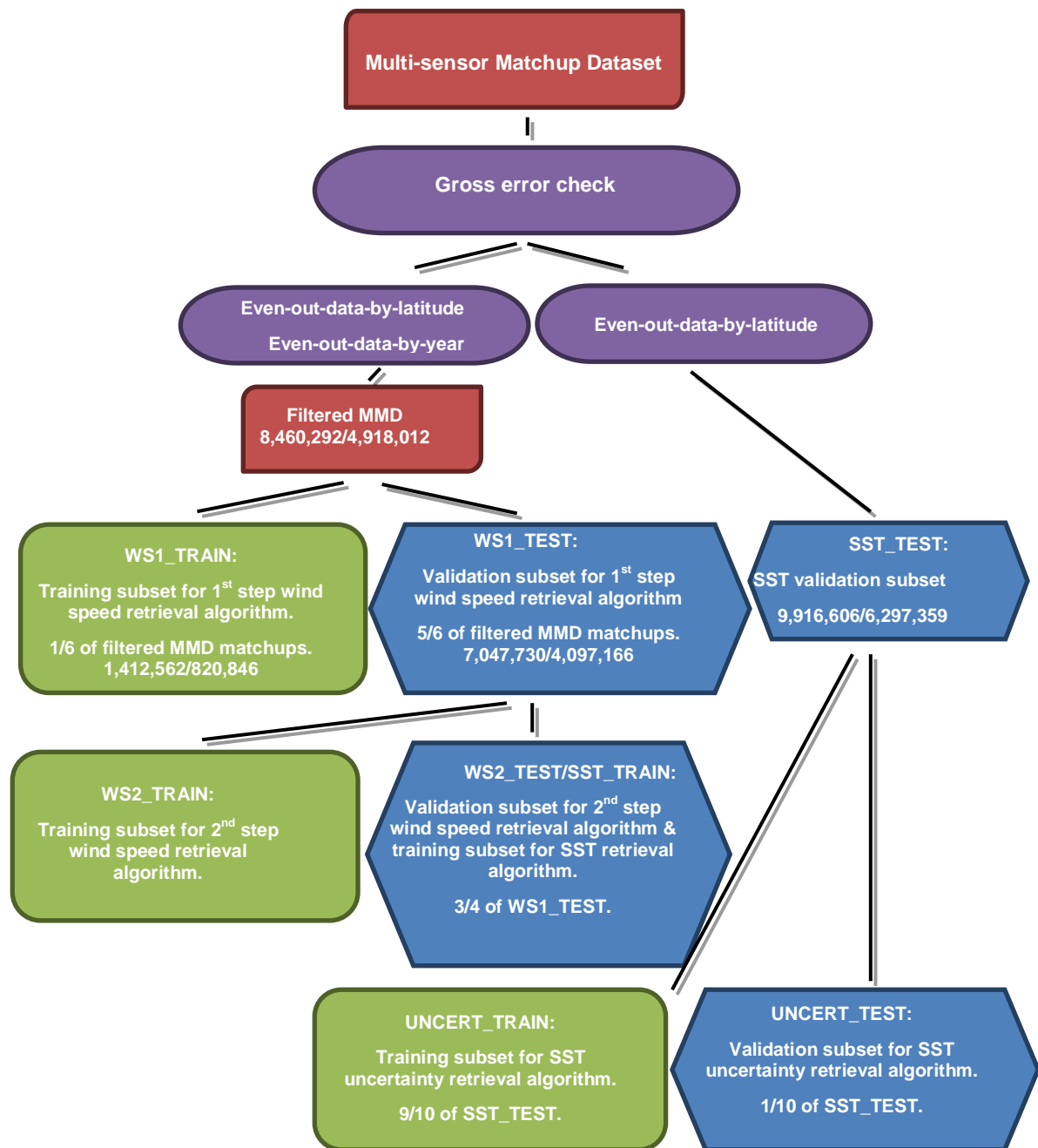


Figure 1: Schematic of the subset division for the AMSR-E and AMSR2 MMDs. The numbers denote the total number of matchups in each AMSR-E/AMSR2 subset.

The geographical distribution of matchups per square kilometre and the latitudinal distribution of drifter matchups for the combined AMSR-E and AMSR2 SST_TEST subsets are shown in Figure 2. The number of matchups per year is shown in Figure 3. Figure 2 demonstrates the spatial distribution of the in situ matchup database, with the North Atlantic Ocean having the largest number of collocations and the Indian Ocean the least. The annual distribution of matchups (Figure 3) shows few matchups in 2002 and another decrease in 2012. In 2002, AMSR-E data does not start until June, and the instrument failed in October 2011. In 2012, AMSR2 data was first available from July.

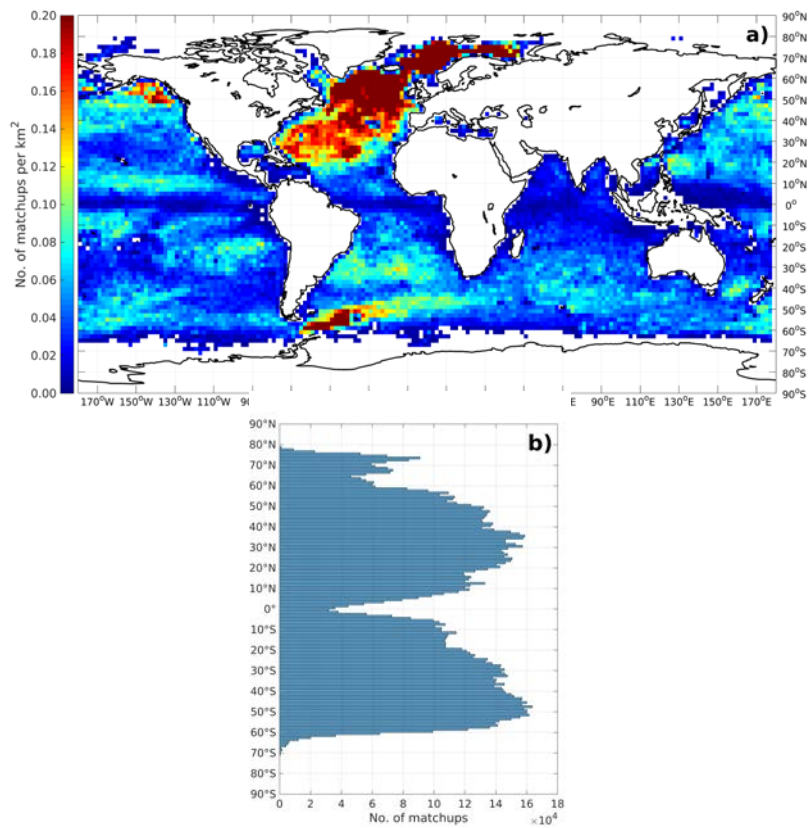


Figure 2: a) Geographical distribution of drifter matchups per square kilometre; and b) latitudinal distribution of drifter matchups for the combined AMSR-E and AMSR2 SST_TEST subsets. The geographical statistics have been gridded using a grid size of 2 degrees, with a minimum of 50 matchups per grid cell.

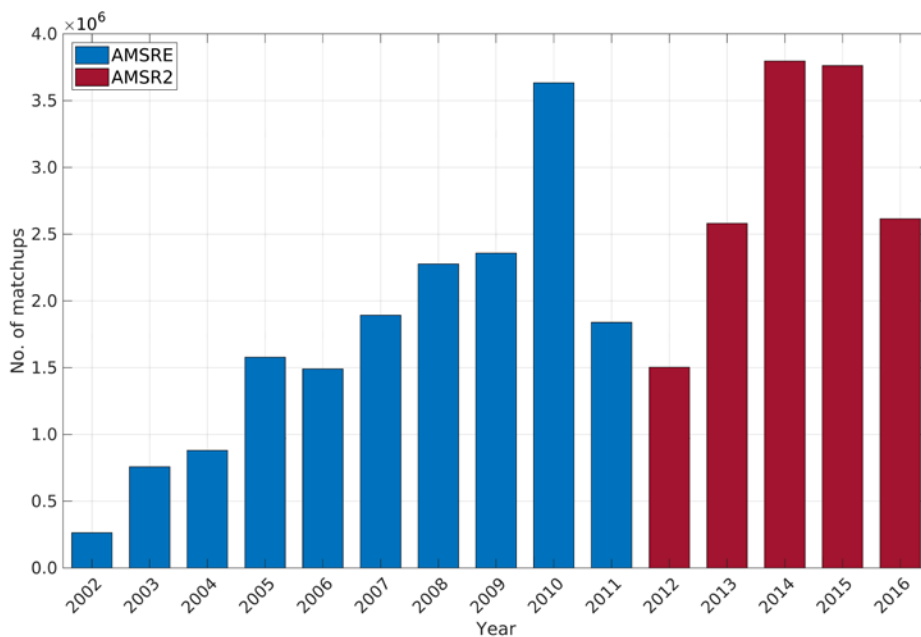


Figure 3: Number of drifter matchups per year for the AMSR-E and AMSR2 SST_TEST subsets.

2.3 Algorithm development

The regression retrieval algorithms described here have been developed within the ESA-CCI SST project to retrieve subskin SST from AMSR-E and AMSR2 and to generate a climate data record of PMW SST for the period June 2002 to October 2017. Two retrieval algorithms have been developed; one for wind speed (WS) and one for SST. A two-step multiple linear regression model is used to retrieve WS given satellite brightness temperatures and NWP fields. In the first stage, a global algorithm is used, whereas in the second stage, specialized algorithms, here for restricted wind speed intervals, are used. The SST retrieval algorithm described here is a two-step multiple linear regression model with specialized retrieval algorithms. In the first stage, the algorithm is trained to perform well over restricted latitude intervals for ascending and descending orbits, respectively, whereas in the second stage, the applied algorithms are specialized for restricted SST and WS intervals, using the first stage retrievals. The specialized algorithms are used to address the non-linearity problem arising from the non-linear relationship between the geophysical parameters in question (SST or WS) and brightness temperature.

2.3.1 WS retrieval algorithm

A global regression model is used in the first stage of the wind speed retrieval process to retrieve an initial estimate of wind speed (WS_a). The definition of “global” is here taken to mean that only one set of regression coefficients is used for all wind speeds. The wind speed retrieval algorithm is inspired by the National Oceanic and Atmospheric Administration (NOAA) AMSR2 wind speed retrieval algorithm (Chang et al., 2015) and expresses wind speed in terms of brightness temperature (T_B) and Earth incidence angle (θ_{EIA})

$$WS_a = a_0 + \sum_{i=1}^{10} (a_{1i}t_i + a_{2i}t_i^2) + a_3\theta \quad (1)$$

where

$$t_i = T_{Bi} - 150 \quad \text{for all channels except the 23.6 GHz channels} \quad (2)$$

$$t_i = \ln(290 - T_{Bi}) \quad \text{for the 23.6 GHz channels} \quad (3)$$

$$\theta = \theta_{EIA} - 55 \quad (4)$$

The coefficients a_0 , a_1 , a_2 and a_3 are regression coefficients, denoted $\mathbf{B}_{\text{global}}$, the summation index i represents the summation over 10 brightness temperature channels; 6.9, 10.7, 18.7, 23.6 and 36.5 GHz (vertical and horizontal polarization), and T_{Bi} denotes the brightness temperature for the i th channel. The regression coefficients are obtained through training on the WS_TRAIN1 subset, using the least-squares method.

The relationship between brightness temperature and wind speed is non-linear and the first-stage retrieval is not able to represent these non-linearities. Hence, a second-stage retrieval needs to be performed where these non-linearities are taken into account. This is done by using specialized wind speed retrieval algorithms. With “specialized” we mean that the algorithm is trained to perform well over specialized domains, in this case over fixed wind speed reference intervals. Hence, one set of regression coefficients, \mathbf{B}_{WS} , is obtained for each reference interval, using the least-squares method. The coefficients are derived through training on subsets of the WS2_TRAIN subset, consisting of a minimum of 50 matchups each. To avoid discontinuities in the retrievals, the wind speed bins were defined with a 50% overlap during training.

The specialized wind speed algorithms are defined for fixed wind speeds in the interval 0 to 20 m s⁻¹, with a bin size of 1 m s⁻¹. This gives a total of 20 specialized wind speed algorithms. When performing the retrieval, regression coefficients are selected from the correct wind speed bin based on the retrieved WS from the first-stage retrieval (WS_a). Like the first-stage retrieval, brightness temperature and incidence angle are used to retrieve the second-stage wind speed

$$WS_{rk} = b_{0k} + \sum_{i=1}^{10} (b_{1ik}t_i + b_{2ik}t_i^2) + b_{3k}\theta \quad (5)$$

where k denotes the reference wind speed bin, ranging from 0 to 20 m s⁻¹, and the coefficients b_0 , b_1 , b_2 and b_3 are regression coefficients, denoted \mathbf{B}_{WS} . The final retrieved wind speed, WS_r, is obtained through linear interpolation between the wind speed obtained for the current WS bin and for the closest neighbouring WS bin.

2.3.2 SST retrieval algorithm

In the first stage of the SST retrieval algorithm, a preliminary estimate of SST (SST_a) is retrieved using a regression model with specialized latitude algorithms for ascending and descending orbits. This means that the algorithm is trained to perform well over fixed reference latitudes and for ascending and descending orbit, respectively. One set of regression coefficients, $\mathbf{B}_{LAT,ORB}$, is therefore obtained for each latitude and for ascending and descending orbits, respectively. The specialized algorithms are derived for reference latitudes in the interval -90 to 90 degrees, with a bin size of 2 degrees, and descending (0) or ascending (1) orbit. This gives a total of 182 specialized latitude and orbit algorithms. As with the specialized WS algorithms, the latitude bins were defined with a 50% overlap during training to avoid discontinuities. For the retrieval process, regression coefficients are selected from the correct latitude and orbit bin using satellite latitude (ϕ_{LAT}) and orbit. The SST retrieval algorithm is inspired by the Remote Sensing System (RSS) AMSR-E SST retrieval algorithm (Wentz and Meissner, 2007). SST is expressed in terms of brightness temperature (T_B), Earth incidence angle (θ_{EIA}), wind speed (WS_r) and the relative angle between satellite azimuth angle and wind direction (ϕ_{REL})

$$SST_{alm} = c_{0lm} + \sum_{i=1}^{12} (c_{1ilm}t_i + c_{2ilm}t_i^2) + c_{3lm}\theta + c_{4lm}WS_r \quad (6)$$

$$+ \sum_{j=1}^2 (c_{5jlm} \cos j\phi_{REL} + c_{6jlm} \sin j\phi_{REL})$$

where

$$t_i = T_{Bi} - 150 \quad \text{for all channels except the 23.6 GHz channels} \quad (7)$$

$$t_i = -\ln(290 - T_{Bi}) \quad \text{for the 23.6 GHz channels} \quad (8)$$

$$\theta = \theta_{EIA} - 55 \quad (9)$$

and l denotes the reference latitude, ranging from -90 to 90 degrees, and m denotes the reference orbit (0 for descending and 1 for ascending orbit). The coefficients c_0 , c_1 , c_2 , c_3 , c_4 , c_5 and c_6 are regression coefficients, denoted $\mathbf{B}_{LAT,ORB}$, the summation index i represents the summation over 12 brightness temperature channels; 6.9, 10.7, 18.7, 23.6, 36.5 and 89.0 GHz (dual polarization), and T_{Bi} denotes the brightness temperature for the i th channel. The regression coefficients are obtained through training on subsets of the

SST_TRAIN subset, consisting of a minimum of 100 matchups each. The least-squares method is used to derive the coefficients. To avoid discontinuities in the retrieval, the final preliminary retrieved SST is obtained through linear interpolation of the SST retrieved for the current latitude and orbit bin and the SST retrieved using the closest latitude and orbit bin.

Wind speed influences the sea surface roughness, which affects the emissivity and therefore also the brightness temperature. To account for this non-linear dependence and the non-linear dependence of brightness temperature on SST, a second-stage SST retrieval is performed. Here, a regression model with specialized SST and WS algorithms is used to retrieve SST. The specialized algorithms are defined for reference SSTs in the interval -2 to 34°C, with a bin size of 2°C, and reference wind speeds in the interval 0 to 20 m s⁻¹, with a bin size of 2 m s⁻¹. This gives a total of 209 specialized SST and WS algorithms. The SST and WS bins were defined with a 1 m s⁻¹ and 1°C overlap, respectively, during training to avoid discontinuities in the retrieval. When performing the retrieval, the correct regression coefficients are found based on retrieved wind speed (WS_r) and first-stage retrieved SST (SST_a). The second-stage SST retrieval algorithm is formulated in the same way as the first-stage retrieval. Brightness temperature, Earth incidence angle, retrieved wind speed and the relative angle between satellite azimuth angle and wind direction are used to retrieve SST

$$SST_{rnp} = d_{0np} + \sum_{i=1}^{12} (d_{1inp}t_i + d_{2inp}t_i^2) + d_{3np}\theta + d_{4np}WS_r \quad (10)$$

$$+ \sum_{j=1}^2 (d_{5jnp} \cos j\phi_{REL} + d_{6jnp} \sin j\phi_{REL})$$

where n denotes the reference SST, ranging from -2 to 34°C, and p denotes the reference wind speed, ranging from 0 to 20 m s⁻¹. The regression coefficients $d_0, d_1, d_2, d_3, d_4, d_5$ and d_6 are referred to as $\mathbf{B}_{SST,WS}$. The specialized algorithms are trained on subsets of the SST_TRAIN subset, consisting of a minimum of 100 matchups each, and the coefficients are obtained using the least-squares method. The final retrieved SST, SST_r, is obtained through bi-linear interpolation between the SST obtained for the current SST and WS bin and for the three closest neighbouring bins.

2.3.3 SST uncertainty retrieval algorithm

An important part of a climate data record is the inclusion and validation of realistic uncertainties. These facilitate the use of the SSTs within ocean and atmosphere models. In this study, we have chosen to follow the approach within the ESA-CCI SST project (Rayner et al., 2015), where the total uncertainty is a combination of three uncertainty components, each with different characteristics. The total uncertainty for the retrieved SST, ϵ_{SSTr} , is thus divided into three independent components; a random component (ϵ_{random}) a local systematic component (ϵ_{local}) and a global systematic component (ϵ_{global}). The total uncertainty is given by

$$\epsilon_{SSTr} = \sqrt{\epsilon_{random}^2 + \epsilon_{local}^2 + \epsilon_{global}^2} \quad (11)$$

These three components have been chosen due to their different behaviour when aggregating the observations. When aggregating in time or space, it is assumed that ϵ_{random} will reduce as $1/\sqrt{N}$, where N is the number of observations. Similarly, ϵ_{local} will reduce as $1/\sqrt{N^*}$ where N^* is the effective number of observations, taking into account a synoptic timescale of 2-5 days and spatial distances of 500-1,000 km. The ϵ_{global} component is

assumed to be systematic and not to be reduced, even for large spatial and temporal averaging scales.

Both the local systematic uncertainty component and the random uncertainty component are obtained through the use of a global regression model. The global systematic uncertainty component, on the other hand, is assumed to be small and therefore set to zero. The retrieval algorithms for the local systematic and random uncertainty components express the uncertainty in terms of retrieved SST (SST_r), retrieved wind speed (WS_r), latitude (ϕ_{LAT}), and solar zenith angle (θ_{SZA})

$$\begin{aligned} \varepsilon_{SST} = & e_0 + e_1SST_r + e_2SST_r^2 + e_3WS_r + e_4WS_r^2 + e_5\theta_{SZA} + e_6\theta_{SZA}^2 \\ & + \sum_{p=1}^4 \left(e_{7p} \cos\left(\frac{\phi_{LAT}}{p}\right) + e_{8p} \sin\left(\frac{\phi_{LAT}}{p}\right) \right) \end{aligned} \quad (12)$$

where the coefficients e_0 , e_1 , e_2 , e_3 , e_4 , e_5 , e_6 , e_7 and e_8 are regression coefficients, determined through training on the UNCERT_TRAIN subset. Two different sets of regression coefficients are obtained; one for the local systematic uncertainty component (\mathbf{B}_{local}) and one for the random uncertainty component (\mathbf{B}_{rnd}).

The uncorrelated uncertainty is used to represent the uncertainty due to radiometric noise, which is represented by the noise equivalent differential temperature (NEdT). To estimate the uncertainty due to uncorrelated effects, an NEdT of 0.1 K (Wentz and Meissner, 2000) was propagated through the retrieval algorithm and a new set of SSTs was generated ($SST_{r,md}$). Hereafter, a pre-binning was performed using the UNCERT_TRAIN subset, where data was binned for retrieved SST, retrieved wind speed, latitude, and solar zenith angle. The intervals and bin sizes used for the pre-binning are shown in Table 3. For each bin, if it consisted of a minimum of 50 matchups, two standard deviations were calculated;

- $\sigma_{\Delta SST_r}$: the standard deviation of the SST_r minus in situ SST difference; and
- $\sigma_{\Delta SST_{r,md}}$: the standard deviation of the SST_r minus $SST_{r,md}$ difference.

The first standard deviation, $\sigma_{\Delta SST_r}$, is used to represent local effects on the total uncertainty and includes drifter uncertainty and sampling effects, whereas the second standard deviation, $\sigma_{\Delta SST_{r,md}}$, is used to represent random and uncorrelated effects. To obtain regression coefficients for the random uncertainty component, the retrieval algorithm was trained against $\sigma_{\Delta SST_{r,md}}$. For the local systematic uncertainty component, the retrieval algorithm was trained against the part of the uncertainty attributed only to local variations, σ_{local} . Hence both sampling effects and drifter uncertainty needed to be removed from $\sigma_{\Delta SST_r}$, in order to only get the local variations. The drifter uncertainty was set to 0.2 K whereas the sampling effect was calculated as a function of latitude. The sampling effect in this context was assumed to be primarily spatial (Høyer et al., 2012) and has been estimated by calculating the pixel-to-footprint variability for one year of GHRSSST Level 4 DMI_OI Global Foundation Sea Surface Temperature Analysis (DMI, 2007).

Table 3: Pre-binning intervals and bin sizes for the uncertainty retrieval training dataset, UNCERT_TRAIN.

Variable	Bin size	Min	Max
Retrieved SST	2°C	-1°C	33°C
Retrieved WS	2 m s ⁻¹	1 m s ⁻¹	19 m s ⁻¹
Latitude	10°	-85°	85°
Solar zenith angle	15°	7.5°	172.5°

2.3.4 Improved RFI mask

Radio Frequency Interference (RFI) is a rapidly increasing problem for geophysical SST and WS retrievals using 6.9, 10.7 and 18.7 GHz. While these are protected frequencies for scientific use (International Telecommunication Union, 2012), the bandwidth of these channels exceed the protected bands. RFI can be divided into three categories (in order of occurrence); space-based ocean-reflected, satellite-to-satellite interference and ground-based RFI. The main source of surface reflected space-based RFI is media broadcasts (TV and radio) from geostationary satellites and satellite downlinks, which affect mostly the 6.9, 10.7 and 18.7 GHz channels. Satellite-to-satellite RFI is a growing problem with an unclear solution. Ground-based RFI is related to land-based microwave link communication systems on oil rigs, near cities, and in regions with military activities and mostly affects the 6.9 GHz channel.

Gentemann and Hilburn (2015) developed an RFI mask which uses observation location and geostationary reflection latitude and longitude to check for RFI contamination. This method was used as an initial RFI mask to screen for potentially contaminated RFI matchups in the data filtering process (Section 3.2.5.2). Here we present an alternative RFI filtering method, based on two additional SST retrieval algorithms. The two new algorithms are formulated exactly as the baseline algorithm with the exception that one excludes the 10 GHz channels (-10GHz algorithm) and the other excludes the 18 GHz channels (-18GHz algorithm). As for the baseline retrieval algorithm, the two-step regression model is used to retrieve SST for the -10GHz and -18GHz algorithms. Even though the 6.9 GHz channels are the ones that are most affected by RFI, we do not exclude them because this could introduce a strong SST dependency in the filter due to the large temperature variation in the sensitivity of the 10 GHz channel (Gentemann et al., 2010). Figure 4 shows the performance of the baseline retrieved AMSR-E PMW SST as a function of the difference between the AMSR-E PMW SST retrieved using the -18GHz algorithm and the baseline retrieved AMSR-E PMW SST.

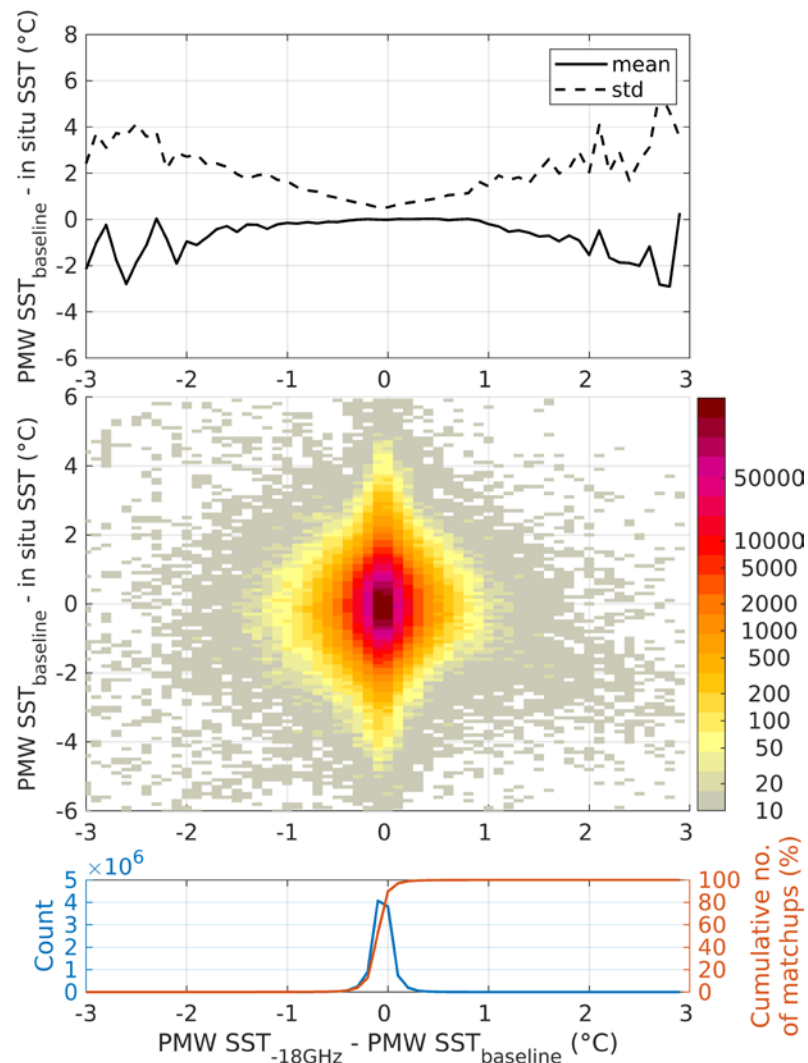


Figure 4: Baseline retrieved AMSR-E PMW SST minus in situ SST as a function of -18GHz retrieved AMSR-E PMW SST minus baseline retrieved AMSR-E PMW SST. Top panel shows the mean (solid) and standard deviation (dashed) of differences for each bin. The heat plot in the mid panel shows the distribution of matchups, and the bottom panel shows the number of matchups (blue) and the cumulative number of matchups (orange) in each bin. A minimum of 10 matchups per bin was used for the statistics calculation.

The standard deviation of baseline retrieved PMW SST minus in situ SST increases as the difference between the -18GHz retrieved PMW SST and the baseline retrieved PMW SST grows, with the largest values found at the tails of the distribution. Furthermore, the magnitude of the mean also increases with increasing difference between the -18GHz retrieved PMW SST and the baseline retrieved PMW SST. The behaviour for the dependence of the SST difference against -10GHz retrieved PMW SST minus baseline retrieved PMW SST are similar and are therefore not shown. Similarly, the results for the AMSR2 retrievals resemble those for the AMSR-E retrievals and are therefore not included here.

Based on these results, a new RFI mask is proposed. The new mask uses a 3- σ filter to detect RFI and flag data if any of the following expressions is true

$$\left| (SST_{r,\text{baseline}} - SST_{r,-10\text{GHz}}) - \mu_{-10\text{GHz}} \right| > 3\sigma_{-10\text{GHz}} \quad (13)$$

$$\left| (SST_{r,\text{baseline}} - SST_{r,-18\text{GHz}}) - \mu_{-18\text{GHz}} \right| > 3\sigma_{-18\text{GHz}} \quad (14)$$

where $SST_{r,-10\text{GHz}}$, $SST_{r,-18\text{GHz}}$ and $SST_{r,\text{baseline}}$ are the final retrieved SST using the -10GHz, -18GHz and baseline algorithms, respectively. $\mu_{-10\text{GHz}}$ and $\mu_{-18\text{GHz}}$ denote the mean of the difference $SST_{r,-10\text{GHz}} - SST_{r,\text{baseline}}$ and $SST_{r,-18\text{GHz}} - SST_{r,\text{baseline}}$, respectively, whereas $\sigma_{-10\text{GHz}}$ and $\sigma_{-18\text{GHz}}$ denote the standard deviation of the corresponding differences. Hereafter, when referring to the baseline retrieved PMW SST we will drop the reference to the retrieval algorithm and simply write PMW SST. The mean and standard deviation of differences used for the proposed RFI mask are shown in Table 4.

Table 4: Mean and standard deviation of differences for retrieved SSTs using the -10GHz and -18GHz algorithm minus baseline retrieved SST for AMSR-E and AMSR2.

Sensor	$\mu_{-10\text{GHz}}$ (K)	$\mu_{-18\text{GHz}}$ (K)	$\sigma_{-10\text{GHz}}$ (K)	$\sigma_{-18\text{GHz}}$ (K)
AMSR-E	0.0024	0.0071	0.192	0.138
AMSR2	-0.0087	0.0043	0.170	0.130

Figure 5a) and b) show the geographical distribution of the gridded mean and standard deviation of the combined AMSR-E and AMSR2 PMW SST minus in situ SST without application of an RFI mask. The region with a strong negative bias and a high standard deviation over Western Europe is a well-known region with large RFI contamination, both from space-based and ground-based RFI sources. The effect of RFI in this region here results in colder PMW SSTs compared to in situ SSTs. Ascension Island is another well-known region which is strongly influence by ground-based RFI, as is most evident in the increased standard deviation but also in the slightly negative mean. Yet another region which is well-known for being contaminated by RFI is the Mediterranean Sea, where the RFI contamination here results in warmer PMW SSTs compared to in situ SSTs. The application of the proposed RFI mask successfully removes RFI in all of the above-mentioned regions, as is evident in Figure 5c) and d). For comparison, Table 4 shows the performance of the SST retrieval algorithm with and without application of the new RFI mask. Application the proposed RFI mask results in a decrease of the standard deviation of the PMW SST minus in situ SST difference by 0.02 and 0.03 K for AMSR-E and AMSR2, respectively, compared to without application of an RFI mask. Hereafter, the new RFI mask has been used instead of the initial mask.

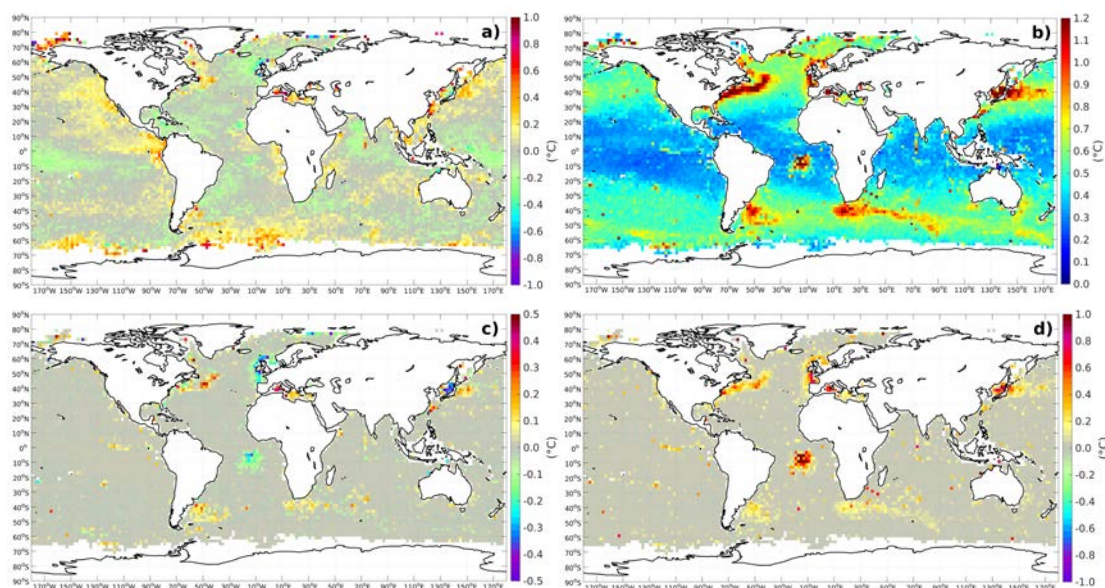


Figure 5: Top panel shows the geographical distribution of a) mean and b) standard deviation of AMSR-E and AMSR2 PMW SST minus in situ SST without application of an RFI mask. Bottom panel shows the distribution of c) mean and d) standard deviation of the difference between the AMSR-E and AMSR2 PMW SST and in situ SST without RFI mask minus the SST difference with the proposed RFI mask. The statistics have been gridded using a grid size of 2 degrees, with a minimum of 50 matchups per grid cell.

Table 5: Mean and standard deviation of PMW SST minus in situ SST, number of matchups removed by the RFI mask and the total number of matchups left in the drifter validation subset, SST_TEST, after all checks have been performed (see Section 3.2.5.2). Additional filtering was performed after application of the RFI mask to exclude obvious erroneous retrievals. Retrievals with a PMW SST outside the accepted range (-2 to 34°C) or with a PMW WS outside the accepted range (0 to 20 m s⁻¹) were therefore excluded.

Sensor	RFI mask	Mean (°C)	Std (°C)	No. of matchups removed by RFI filter	No. of matchups
AMSR-E	No RFI mask	-0.012	0.54	-	10,067,979
	3- σ filter	-0.0099	0.52	154,344	9,916,606
AMSR2	No RFI mask	0.0027	0.54	-	6,384,638
	3- σ filter	0.0067	0.51	107,096	6,297,359

2.4 Results

The filtering steps described in Section 3.2.5.2 and the RFI mask described in Section 3.3.4 only ensures that the input data to the retrieval algorithm is of sufficient quality. It is also important to ensure that the retrievals used in the validation are of sufficient quality and to flag erroneous output. Therefore, additional filtering was performed where PMW SST retrievals outside the accepted range (-2 to 34°C) and PMW WS retrievals outside the accepted range (0 to 20 m s⁻¹) were flagged as erroneous. The results shown in this section include the filtering steps outlined in Section 3.2.5.2, but with the new RFI mask instead of the initial one, as well as the checks on the retrieval output as outlined above. For the generation of the climate data record, the PMW SST retrievals follow the GHRSSST GDS 2.0 data specification (GHRSSST Science Team, 2010) for L2P and each retrieval has been assigned a quality level from 0 (no data) to 5 (best quality) to indicate the quality of the

individual retrievals. Quality levels are defined by producers relative to the characteristics of a given data stream. Table 6 shows the definition of the rules applied for different quality levels in this case.

Table 6: Definition of quality levels and rules for assignment.

Quality Level	Definition	Rules
0	No data	
1	Bad data	Quality controls and various checks for atmospheric and surface effects (see Section 3.2.5.2)
2	Worst-quality usable data	<ul style="list-style-type: none"> • SST uncertainty ≥ 1 • Proximity to sea ice • Proximity to land
3	Low quality	$0.5 < \text{SST uncertainty} < 1$
4	Acceptable quality	$0.35 < \text{SST uncertainty} \leq 0.5$
5	Best quality	$\text{SST uncertainty} \leq 0.35$

The quality controls and various checks for surface and atmospheric effects referred to in the definition of quality level 1 are the same as the filtering procedures defined in Section 3.2.5.2 (new RFI mask instead of initial mask), with few exceptions. The quality level 1 check for the PMW SST CDR retrievals does not include a check for diurnal warming effects. On the other hand, it includes an additional check where the retrieved SST is compared to a background SST. If the retrieved SST deviates more than 10°C from the background, the retrieval is assigned quality level 1. Quality level 2 PMW SST retrievals in the CDR are assigned based on the total SST uncertainty and on an extended sea ice and land mask, which is based on the proximity of the retrieval to sea ice and land. Due to the construction of the MMD, the sea ice and land masking performed here does not fully correspond to the extended sea ice and land mask used in the generation of the CDR. Therefore, the filtering performed for the MMDs approximately corresponds to excluding quality level 1 and 2 data and only retaining quality level 3 to 5 data.

The regression retrieval has been run for the AMSR-E and AMSR2 validation subsets (SST_TEST) defined in Section 3.2.5.2. The overall summary statistics of the PMW SSTs against drifter in situ SSTs for different quality levels are shown in Table 6. The AMSR-E quality level 3-5 PMW SSTs give a bias -0.01 K and standard deviation of 0.52 K when compared against in situ SSTs. By contrast, the quality level 4 and 5 AMSR-E retrievals give SSTs with a bias of -0.02 K and a standard deviation of 0.46 K. Comparing the AMSR2 quality level 3-5 PMW SSTs against in situ SSTs gives a bias of 0.007 K and a standard deviation of 0.51 K. The mean and standard deviation of the AMSR2 quality level 4 and 5 PMW SST retrievals are smaller, 0.002 K and 0.45 K, respectively.

To obtain a completely independent validation, the retrieved SSTs were also validated against SSTs from Argo floats. The Argo floats are not as numerous as the drifters and therefore, the AMSR-E and AMSR2 Argo validation subsets only consist of 148,895 and 154,715 matchups, respectively. The comparison of AMSR-E and AMSR2 quality level 4 and 5 retrievals against Argo SSTs shows a slightly better performance than the comparison with drifters. The AMSR-E quality level 4 and 5 retrievals give a bias of -0.009 K and a standard deviation of 0.44 K when compared against Argo floats. Similarly, comparing the AMSR2 quality level 4 and 5 PMW SSTs against Argo floats gives a bias of 0.01 K and a standard deviation of 0.43 K.

Table 7: Performance of the SST retrieval algorithm for AMSR-E and AMSR2 drifter and Argo subsets. The table shows the mean and standard deviation of PMW SST minus in situ SST and number of matchups contributing to the statistics for different subsets.

Sensor	Quality level	Mean Drifter (K)	Std Drifter (K)	No. of matchups	Mean Argo (K)	Std Argo (K)	No. of matchups
AMSR-E	3	0.02	0.64	2,763,087	0.007	0.62	39,939
	4	-0.01	0.51	4,399,894	-0.002	0.50	60,398
	5	-0.03	0.37	2,753,625	-0.02	0.36	48,558
	3-5	-0.01	0.52	9,916,606	-0.004	0.50	148,895
	4-5	-0.02	0.46	7,153,519	-0.009	0.44	108,956
AMSR2	3	0.02	0.64	1,729,073	0.03	0.62	37,273
	4	0.006	0.52	2,549,348	0.02	0.51	57,343
	5	-0.003	0.35	2,000,938	0.004	0.34	60,089
	3-5	0.007	0.51	6,279,359	0.02	0.48	154,705
	4-5	0.002	0.45	4,550,286	0.01	0.43	117,432

Figure 6 shows the geographical distribution of the gridded mean and standard deviation of the AMSR-E and AMSR2 PMW SST minus drifter in situ SST based on the combined AMSR-E and AMSR2 SST_TEST subsets, consisting of in total 16,195,965 drifter matchups. The distribution of the mean shows a positive bias for high latitudes, especially in the southern hemisphere. This has been confirmed to be linked to undetected sea ice. Furthermore, a warm bias is seen for the west coast of America and the east coast of Asia. A negative bias is seen for e.g. the Pacific warm pool area and the Arabian Sea. No clear latitudinal dependence can be discerned for the mean. However, for the geographical distribution of the standard deviation a latitudinal dependence is observed. Lower standard deviations are found at low latitudes and higher standard deviations at higher latitudes. Furthermore, higher standard deviation is observed in the dynamical ocean regions, such as the Kuroshio Current, the Gulf Stream Extension and the Agulhas Current. These are highly dynamical regions with large SST gradients over smaller scales. When the large satellite footprint (43x75 km and 35x62 km for the AMSR-E and AMSR2 6.9 GHz resolution, respectively) is compared against in situ SST observations, which are point measurements, the SST difference is enhanced. Hence, the higher standard deviations in these regions are not a measure of the quality of the PMW SST retrievals but rather related to the large SST variability in these regions.

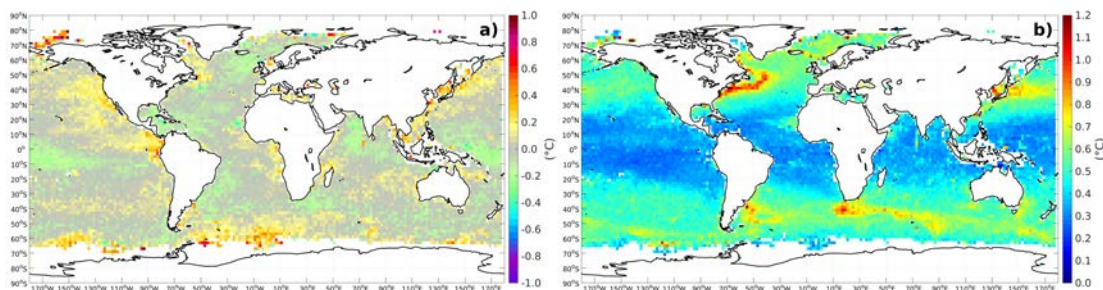


Figure 6: The geographical distribution of a) mean and b) standard deviation of AMSR-E and AMSR2 PMW SST minus drifter in situ SST. The statistics have been gridded using a grid size of 2 degrees, with a minimum of 50 matchups per grid cell.

The performance of the PMW SST against drifter in situ SST as a function of SST, wind speed and latitude has been investigated (Figure 7 - Figure 9). A dependence can be seen for both cold and warm SSTs. The warm bias for cold SST (SSTs < 0°C) was investigated and found to be related to sea ice contamination. The reason for the cold bias for warm SST (SST > 29°C) is not yet understood. The standard deviation, on the other hand, decreases with warmer SST. Wind speed affects the sea surface roughness, which impacts the emissivity of the ocean and therefore also the brightness temperature in the retrievals. The dependence of the retrieved SST on wind speed therefore reflects the dependence on sea surface roughness. The binned statistics of the performance against wind speed shows a cold bias for wind speeds in the range 5-8 m s⁻¹ and otherwise a small warm bias for both high and low wind speeds. The standard deviation is lowest for low wind speeds and increases for increasing wind speeds. As was evident in the geographical distributions of the gridded statistics (Figure 6) a latitudinal dependence is seen for the SST performance against in situ SSTs. Lower standard deviation is found at lower latitudes and higher standard deviation is found for higher latitudes. A cold bias is seen for matchups located between 15°S and the equator, which corresponds to the cold bias seen for the Pacific warm pool area. The negative bias seen for matchups centered around 60°N corresponds to the cold bias seen just south of Iceland, in the North Atlantic Ocean. Furthermore, a warm bias is seen for matchups at the higher latitudes. This has been confirmed to be an effect of sea ice contamination.

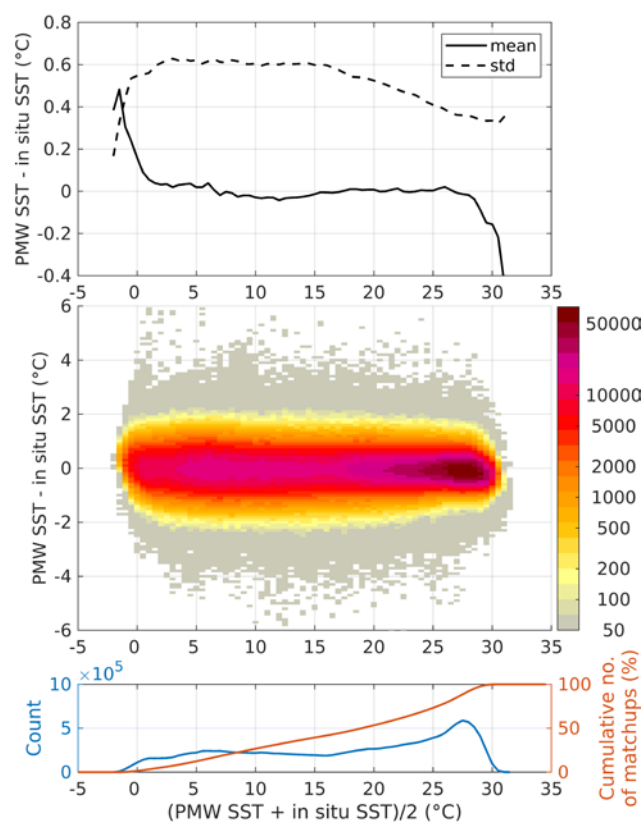


Figure 7: AMSR-E and AMSR2 PMW SST minus drifter in situ SST as a function of average SST $((\text{PMW SST} + \text{in situ SST})/2)$. Top panel shows the mean (solid) and standard deviation (dashed) of differences for each bin. The heat plot in the mid panel shows the distribution of matchups, and the bottom panel shows the number of matchups (blue) and the cumulative number of matchups (orange) in each bin. A minimum of 50 matchups per bin was used for the statistics calculation.

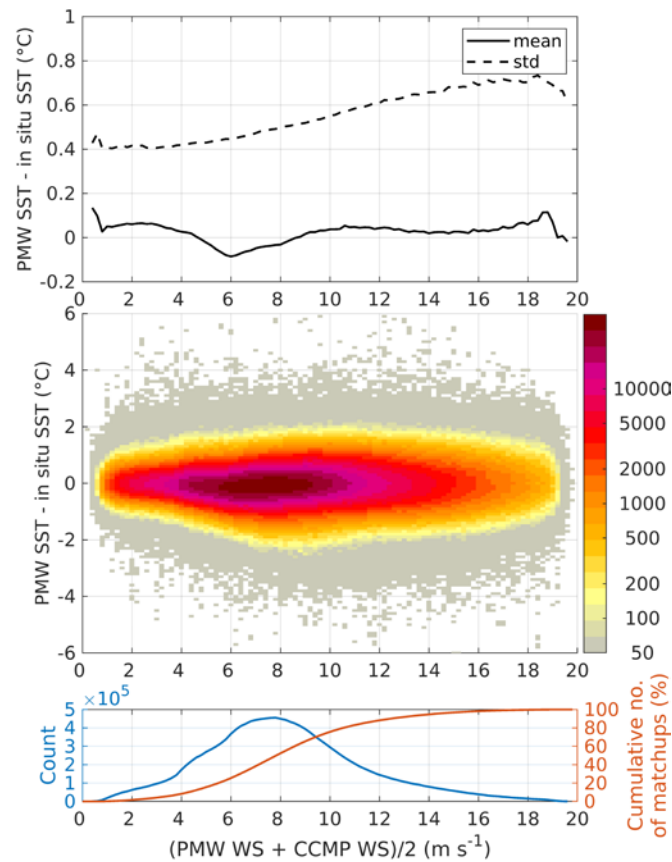


Figure 8: AMSR-E and AMSR2 PMW SST minus drifter in situ SST as a function of average WS ((PMW WS + CCMP WS)/2). Top panel shows the mean (solid) and standard deviation (dashed) of differences for each bin. The heat plot in the mid panel shows the distribution of matchups, and the bottom panel shows the number of matchups (blue) and the cumulative number of matchups (orange) in each bin. A minimum of 50 matchups per bin was used for the statistics calculation.

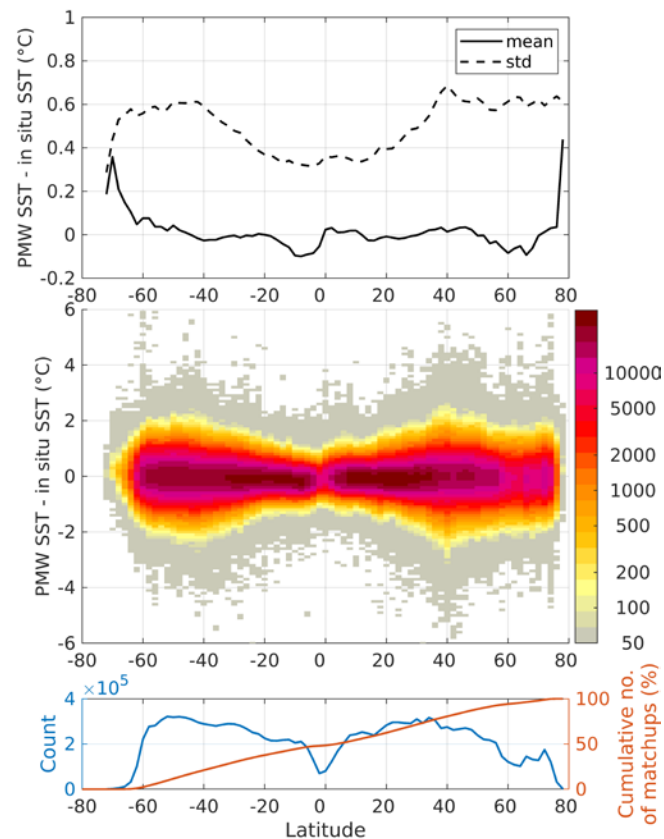


Figure 9: AMSR-E and AMSR2 PMW SST minus drifter in situ SST as a function of latitude. Top panel shows the mean (solid) and standard deviation (dashed) of differences for each bin. The heat plot in the mid panel shows the distribution of matchups, and the bottom panel shows the number of matchups (blue) and the cumulative number of matchups (orange) in each bin. A minimum of 50 matchups per bin was used for the statistics calculation.

2.4.1 Sensitivity

The sensitivity of the retrieved SST with respect to changes in true sea surface temperature was investigated (Merchant et al., 2009). A subset of AMSR-E versus drifter matchups for the year 2010, consisting of 4,642,710 good drifter matchups, was used to generate two sets of simulated brightness temperatures. The simulated brightness temperatures were generated using an updated version of the forward model developed by Wentz and Meissner (2000), as described in Nielsen-Englyst et al. (2018). Both sets use WS, TCLW and TCWV input from NWP and SST input from drifting buoys. The first set was simulated with in situ SST plus 1°C, while the second set of brightness temperatures was simulated with in situ SST minus 1°C, with NWP input held constant for both sets. The resulting brightness temperatures were subsequently propagated through the regression retrieval algorithm to derive the corresponding SST-1 and SST+1 estimates. The sensitivity was then calculated based on the retrieved SSTs and the overall mean sensitivity was estimated to 0.90.

The geographical distribution of sensitivity is shown in Figure 10. The sensitivity is mostly larger than 0.85 but there are areas with lower sensitivity, such as the Pacific warm pool

area and the Arabian Sea, with minimum sensitivities just below 0.5. The Pacific warm pool area is characterized by high TCWV content, whereas the Arabian Sea is a relatively dry area in comparison. There are also areas of relatively lower sensitivity, such as south of Greenland and in a belt around Antarctica. These regions are characterized by high wind speeds, persistent cloud cover and rain. The dependence of the sensitivity on TCWV, TCLW and WS was investigated (not shown). A small dependence for very high TCWV was found but nothing for TCLW or WS. The geographical distribution of sensitivity for the initial estimate of SST (i.e. the latitude and ascending/descending retrieval), was also investigated to see if an explanation for the low sensitivity could be found. In addition, a global regression model, using the same regression algorithm, but with only one set of regression coefficients for all data (i.e. without any binning), was used to estimate the sensitivity. For the latitude and ascending/descending retrieval, lower sensitivities were found in a narrow band just north of the Equator, as well as for high latitudes (not shown). The global model exhibited highest sensitivities for low latitudes, with lower sensitivities for lower latitudes (not shown). Based on this, we reason that the low sensitivities seen for the two-stage retrieval algorithm are primarily an artefact of the binning performed in the retrieval. The binning performed in both the first-stage and second-stage retrievals might result in bins with very small SST variability. For these bins, e.g. wind speed and water vapour might vary more and thus the regression algorithm will instead correct for those contributions. Hence, the sensitivity of the algorithm to changes in true SST will be lower.

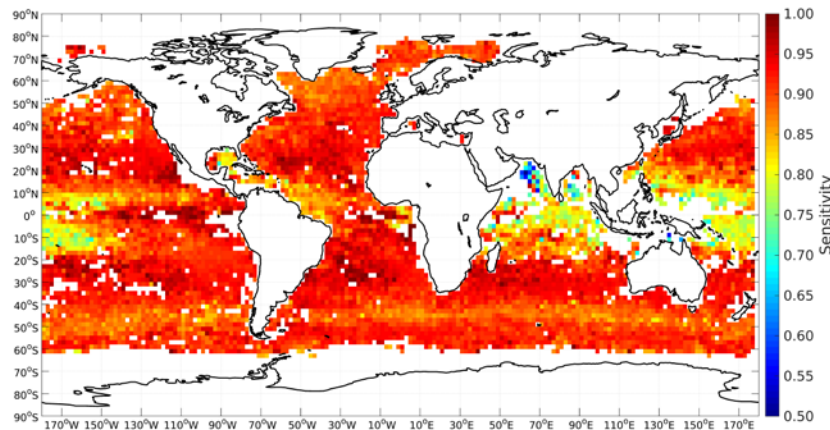


Figure 10: The geographical distribution of sensitivity with respect to changes in SST for an AMSR-E subset consisting of matchups from year 2010. The statistics have been gridded using a grid size of 2 degrees, with a minimum of 50 matchups per grid cell.

2.4.2 SST uncertainty

Validation of the derived uncertainty is essential for the usefulness of the uncertainty estimate. Here, the satellite SST retrievals versus drifter in situ observations have been used for validating the total uncertainty estimates. Only independent drifter matchups have been used for the validation. Figure 11 shows the observed AMSR-E and AMSR2 PMW SST uncertainty against drifters versus the modelled uncertainty, i.e. the estimated PMW SST uncertainty (see Section 3.3.3). The ideal uncertainty is given by the dashed lines, which on top of satellite SST uncertainty, also includes the drifter in situ uncertainty and sampling effects. The drifter uncertainty is estimated to 0.2 K whereas the sampling effect is defined as a latitude dependent function. As shown in Høyer et al. (2012), the sampling effect is primarily spatial, with only a small temporal component. Based on this, the sampling effect has been estimated using the pixel-to-footprint variability for one year of GHRSSST Level 4 DMI_OI Global Foundation Sea Surface Temperature Analysis (DMI, 2007). The mean retrieved AMSR-E and AMSR2 SST uncertainty is estimated to 0.42 K and 0.41 K, respectively. The validation results for the observed satellite SST uncertainties show good agreement with the retrieved uncertainties (see Figure 11).

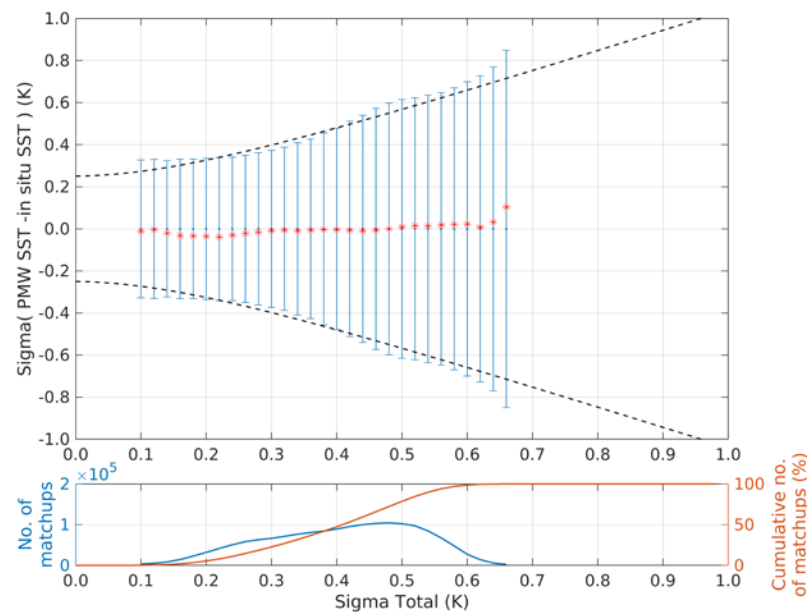


Figure 11: AMSR-E and AMSR2 PMW SST uncertainty validation against drifter in situ SST. The top panel shows the observed PMW SST minus drifter in situ SST uncertainty versus the modelled uncertainty, i.e. the retrieved PMW SST uncertainty. The dashed lines indicate the ideal uncertainty, in which drifter SST uncertainty and sampling errors have been included. The red asterisks denote the mean bias and the solid blue lines mark one standard deviation of the PMW SST minus drifter in situ SST difference for each 0.02 K bin. The bottom panel shows the number of matchups (blue) and the cumulative percentage of matchups (red) per bin.

2.4.3 Time consistency

The temporal stability in a climate data record is essential for later use and analysis. As the algorithms for the two satellite datasets have been derived using the same reference in situ dataset (drifting buoys), we expect that there are no large inconsistencies between the two datasets. Figure 12 shows the seasonal averaged independent validation statistics. It is clear from the figure that the performance of the two datasets is very similar. One excursion is the beginning of the AMSR2 period, where we see a cold bias larger than 0.1 degrees. The reason for this is not clear to us. RFI and geographical sampling effects were investigated but not found to be responsible for this deviation.

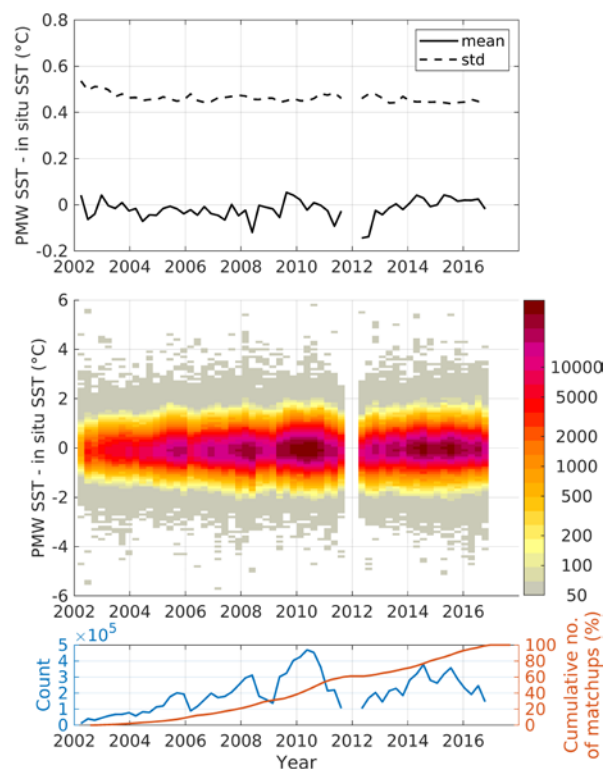


Figure 12: AMSR-E and AMSR2 quality level 4 and 5 PMW SST minus drifter in situ SST as a function of time (season). Top panel shows the mean (solid) and standard deviation (dashed) of differences for each bin. The heat plot in the mid panel shows the distribution of matchups, and the bottom panel shows the number of matchups (blue) and the cumulative number of matchups (orange) in each bin. A minimum of 50 matchups per bin was used for the statistics calculation.

2.5 Discussion

In the retrieval presented above, we train and test our wind speeds against the CCMP winds that are based upon observations from passive and active Microwaves (see e.g. Atlas et al., 2011). This implies that information from the AMSR-E and AMSR2 are already included in the CCMP and that it cannot be regarded as a truly independent wind estimate. However, since the CCMP also includes a lot of information from other sensors, such as in situ observations and models, we decided to use this product for the algorithm validation, as it gave significantly better SST results, when we used the CCMP winds than using the ERA Interim wind speeds.

The global SST validation results with a standard deviation of 0.46 and a bias of -0.02 for quality level 4 and 5 retrievals are comparable to or even better than previous validations of AMSR-E PMW SST retrievals (Gentemann, 2014; O'Carroll et al., 2008). Validation results for quality level 4 and 5 AMSR2 retrievals give SSTs with a bias of 0.002 K and a standard deviation of 0.45 K. Gentemann and Hilburn (2015) reported a standard deviation of 0.55 K and a bias of -0.02 K for validation of AMSR2 against in situ buoy measurements for the same period (2012-2016). We have also derived an uncertainty for each PMW SST retrieval and the uncertainty validation results against in situ measurements indicate a good agreement, with an uncertainty of 0.42 K and 0.41 K for AMSR-E and AMSR2 PMW retrievals, respectively. The modelled uncertainties, including the in situ uncertainty and sampling effects are estimated to 0.45 K and 0.44 K for AMSR-E and AMSR2 quality level 4 and 5 retrievals, respectively.

The performance of the SST retrieval algorithm shows a latitudinal dependence in standard deviation, with higher standard deviation for higher latitudes. This is in line with the findings reported in Gentemann (2014). Furthermore, our results show an increase in standard deviation in the dynamical ocean regions, which are regions with large mesoscale activity and large SST variability over smaller scales. This is not believed to be related to the performance of the algorithm, but to sampling errors due to comparison of satellite observations, which have a large footprint, to in situ observations, which are point measurements. It was evident from Figure 6 and Figure 9 that we saw some sea ice contamination in the high latitudes. Due to the construction of the MMD, we were only able to mask out ice within 160 km in the algorithm development and validation, which is probably too low. The effect on the global validation statistics is limited but when generating the full CDR, an ice mask distance of 200 km was chosen to minimize the impact from sea ice. These residual effects from the sea ice could probably be reduced in an algorithm, where the sea ice information is based upon a retrieval using the observations and not relying on an external product. No coastal effects were seen in the validation.

The performance of the PMW SST retrievals is comparable to the good infrared satellite SST retrievals, in particular when the sampling errors are taken into account. The difference in footprint size between the IR (1 km) and the PMW SSTs (40-70 km) will introduce a larger sampling difference. Furthermore, cloud contamination has a significant impact on infrared SST retrievals since IR satellite instruments are unable to see the surface through clouds (e.g. Jones et al., 1996; Reynolds et al., 2002). In addition, both aerosols (Diaz et al., 2001; e.g. Vásquez-Cuervo et al., 2004) and water vapour attenuation (Emery et al., 1994) typically are related to biases in the IR retrievals. PMW SSTs don't suffer from contamination due to either of these factors, but they are limited by precipitating clouds. The availability of PMW SSTs in regions characterized by persistent cloud cover should therefore be much higher than the availability of IR SSTs. Table 1 shows the availability of the PMW SSTs globally. However, the filtering procedure described in Section 3.2.5.2 includes flagging of not only the quality of the satellite data but also flagging based on in situ and auxiliary data, as well as flagging to remove diurnal warming effects. By excluding the filters which do not pertain to the quality of satellite data, the availability of PMW SSTs in the tropical Indian Ocean (80-100°E, 15°S-20°N), which is a region dominated by clouds (Rossow, 1993) and heavy rain (Arkin and Janowiak, 1993), were found to be 71%. This is in line with findings reported by Guan and Kawamura (2003), where the annual mean availability of PMW SSTs in the tropical Indian Ocean was estimated to be 73%. The availability of IR SSTs in the same region was reported to be 35% (Guan and Kawamura, 2003). The performance of the PMW SSTs against drifter in situ observations in this region was found to be -0.04 ± 0.36 K. The majority of matchups were of quality level 5, with only some quality level 4 data.

Ideally, the SST sensitivity should be 1, however, there are several geophysical factors affecting the microwave retrieval, such as water vapour, cloud water and surface roughness (quantified through wind speed). These factors contribute to lower sensitivity to the true SST variations. Nielsen-Englyst et al. (2018) reported sensitivities ranging from 0.4 to up to 0.6, with the lowest values found for high latitudes. Similar results were found by Gentemann et al. (2010). In contrast, we have reported sensitivities ranging from just below 0.5 up to close to 1.0, with the lowest sensitivities found at low latitudes. The reason for the low sensitivity is probably an effect of the binning performed in both the first-stage and the second-stage retrieval. When performing the regression, we divide the data into different bins. If the SST variability within a bin is very small, the algorithm corrects for other factors, such as wind speed (through its impact on surface roughness), water vapour, etc. instead of SST. Hence, the sensitivity to changes in true SST will be lower. Tests using a global coefficients showed a latitudinal pattern in the sensitivity, as expected, with highest sensitivity for warmer waters. The overall sensitivity was, however, lower than what was obtained with the two step algorithm.

The CDR generated here showed a good inter-sensor consistency, as they have been referenced to the same in situ observational network. The use of in situ observations for SST algorithm developments has a risk of introducing biases related to inadequacies in the

observational network. This effect was attempted to be minimized with the geographical even-out-by-latitude and appeared to be small for our algorithm, as the Argo validation confirms the validation from drifting buoys. However, the approach of using physically based retrievals is preferred for the IR retrievals as discussed in (Merchant et al., 2008; Merchant and Le Borgne, 2004) and have also shown promising results for AMSR-E (Nielsen-Englyst et al., 2018). Future developments could include forward modelling in the inter-sensor adjustment and algorithm developments.

A High Priority Candidate Mission (HPCM) called the Copernicus Imaging Microwave Radiometer (CIMR, (Donlon, 2019; Kilic et al., 2018)) is now being studied at the European Space Agency. CIMR proposes a conically scanning radiometer having a swath > 1900 km and will include channels at 1.4 GHz (~60 km), 6.9 and 10.65 GHz (<15 km) 18.8 GHz (5-6 km) and 36.5 GHz (4-5) km on the same platform in a high inclination dawn-dusk orbit coordinated with the MetOp-SG(B) (offering opportunities for synergy with the Microwave Radiometer (MWI) and Scatterometer (SCA)). Our algorithms can easily be adapted to the CIMR frequencies, taking into account the enhanced spatial resolution, improved NEdT and addition of an L-band channel that can help in wind speeds much greater than 20 m s⁻¹.

2.6 Conclusions

Retrieval algorithms have been developed with the purpose of generating an SST climate data record from the AMSR-E and AMSR2 passive microwave satellite observations for the period 2002-2016. The algorithms include WS retrievals and SST retrievals, with corresponding uncertainty retrievals and a new and effective method for detecting and removing RFI contamination. The results show an overall bias and standard deviation for quality level 4 and 5 AMSR-E and AMSR2 PMW SSTs against drifter in situ SSTs of -0.02 ± 0.46 K and 0.002 ± 0.45 K, respectively. The modelled uncertainty, including in situ uncertainty and sampling effects, are estimated to 0.45 K and 0.44 K, respectively. The thorough validation results against independent in situ observations demonstrate that the algorithms developed here generate a consistent climate data record, with very good performance and reliable uncertainty estimates. Furthermore, a sensitivity of 0.9 for the algorithm ensures retrievals that are able to represent the true variability in the SST.

To conclude, the PMW SST CDR record has been shown to provide accurate and consistent SST retrievals which can be used in non-precipitating conditions for global monitoring and assessment of the oceans. With the uncertainties in the funding for future microwave satellite missions, it is therefore highly recommended that a fully operational multi-frequency passive microwave satellite mission, such as CIMR, should be part of the future satellite constellation to monitor the world oceans.

2.7 References

Abraham, J.P., Baringer, M., Bindoff, N.L., Boyer, T., Cheng, L.J., Church, J.A., Conroy, J.L., Domingues, C.M., Fasullo, J.T., Gilson, J., Goni, G., Good, S.A., Gorman, J.M., Gouretski, V., Ishii, M., Johnson, G.C., Kizu, S., Lyman, J.M., Macdonald, A.M., Minkowycz, W.J., Moffitt, S.E., Palmer, M.D., Piola, A.R., Reseghetti, F., Schuckmann, K., Trenberth, K.E., Velicogna, I., Willis, J.K., 2013. A Review of Global Ocean Temperature Observations: Implications for Ocean Heat Content Estimates and Climate Change. *Rev. Geophys.* 51, 450–483. <https://doi.org/0.1002/rog.20022>

Argo, 2018. Argo float data and metadata from Global Data Assembly Centre (Argo GDAC). SEANOE.

Arkin, P.A., Janowiak, J.E., 1993. Tropical and subtropical precipitation, in: Gurney, R.J., Foster, J.L., Parkinson, C.L. (Eds.), *Atlas of Satellite Observations Related to Global Change*. Cambridge University Press, pp. 165–180.

Ashcroft, P., Wentz, F.J., 2013. AMSR-E/Aqua L2A Global Swath Spatially-Resampled Brightness Temperatures, Version 3.

Atkinson, C.P., Rayner, N.A., Kennedy, J.J., Good, S.A., 2014. An integrated database of ocean temperature and salinity observations. *J. Geophys. Res. Ocean.* 119, 7139–7163. <https://doi.org/10.1002/2014JC010053>

Atlas, R., Hoffman, R.N., Ardizzone, J., Leidner, S.M., Jusem, J.C., Smith, D.K., Gombos, D., 2011. A cross-calibrated, multiplatform ocean surface wind velocity product for meteorological and oceanographic applications. *Bull. Am. Meteorol. Soc.* 92, 157–174. <https://doi.org/10.1175/2010BAMS2946.1>

Block, T., Embacher, S., Merchant, C.J., Donlon, C., 2018. High-performance software framework for the calculation of satellite-to-satellite data matchups (MMS version 1.2). *Geosci. Model Dev.* 11, 2419–2427. <https://doi.org/10.5194/gmd-11-2419-2018>

Brasnett, B., Colan, D.S., 2016. Assimilating retrievals of sea surface temperature from VIIRS and AMSR2. *J. Atmos. Ocean. Technol.* 33, 361–375. <https://doi.org/10.1175/JTECH-D-15-0093.1>

Chacko, N., 2017. Chlorophyll bloom in response to tropical cyclone Hudhud in the Bay of Bengal: Bio-Argo subsurface observations. *Deep Sea Res. Part I Oceanogr. Res. Pap.* 124, 66–72.

Chang, P.S., Jelenak, Z., Alsweiss, S., 2015. Algorithm Theoretical Basis Document: GCOM-W1/AMSR2 Day-1 EDR version 1.0.

Dee, D.P., Uppala, S.M., Simmons, A.J., Berrisford, P., Poli, P., Kobayashi, S., Andrae, U., Balmaseda, M.A., Balsamo, G., Bauer, P., Bechtold, P., Beljaars, A.C.M., van de Berg, L., Bidlot, J., Bormann, N., Delsol, C., Dragani, R., Fuentes, M., Geer, A.J., Haimberger, L., Healy, S.B., Hersbach, H., Hólm, E. V., Isaksen, L., Kållberg, P., Köhler, M., Matricardi, M., McNally, A.P., Monge-Sanz, B.M., Morcrette, J.J., Park, B.K., Peubey, C., de Rosnay, P., Tavolato, C., Thépaut, J.N., Vitart, F., 2011. The ERA-Interim reanalysis: Configuration and performance of the data assimilation system. *Q. J. R. Meteorol. Soc.* 137, 553–597. <https://doi.org/10.1002/qj.828>

Diaz, J.P., Arbelo, M., Expósito, F.J., Podestá, G., Prospero, J.M., Evans, R., 2001. Relationship between errors in AVHRR-derived sea surface temperature and the TOMS Aerosol Index. *Geophys. Res. Lett.* 28, 1989–1992.

DMI, 2007. GHRSSST Level 4 DMI_OI Global Foundation Sea Surface Temperature Analysis (GDS version 2). Ver. 1.0.

Donlon, C.J., 2019. Mission Requirements Document for the Copernicus Imaging Microwave Radiometer, v2.0, February 2019, available from the European Space Agency.

Donlon, C.J., Stark, M.M., Roberts-Jones, J., Fiedler, E., Wimmer, W., 2012. The operational sea surface temperature and sea ice analysis (OSTIA) system. *Remote Sens. Environ.* 116, 140–158.

Embury, O., Merchant, C.J., Corlett, G.K., 2012. A reprocessing for climate of sea surface temperature from the along-track scanning radiometers: Initial validation, accounting for skin and diurnal variability effects. *Remote Sens. Environ.* 116, 62–78. <https://doi.org/10.1016/j.rse.2011.02.028>

Emery, W.J., Yu, Y., Wick, G.A., Schuessel, P., Reynolds, R.W., 1994. Correcting infrared satellite estimates of sea surface temperature for atmospheric water vapour attenuation. *J. Geophys. Res. Ocean.* 99, 5219–5236.

Gentemann, C.L., 2014. Three way validation of MODIS and AMSR-E sea surface temperatures. *J. Geophys. Res. Ocean.* 119, 2583–2598. <https://doi.org/10.1002/2013JC009716>

Gentemann, C.L., Donlon, C.J., Stuart-Menteth, A., Wentz, F.J., 2003. Diurnal signals in satellite sea surface temperature measurements. *Geophys. Res. Lett.* 30. <https://doi.org/10.1029/2002GL016291>

Gentemann, C.L., Hilburn, K., 2015. In situ validation of sea surface temperatures from the GCOM-W1 AMSR2 RSS calibrated brightness temperatures: Validation of RSS GCOM-W1 SST. *J. Geophys. Res. Ocean.* 120, 3567–3585. <https://doi.org/10.1002/2014JC010574>

Gentemann, C.L., Meissner, T., Wentz, F.J., 2010. Accuracy of Satellite Sea Surface Temperatures at 7 and 11 GHz. *IEEE Trans. Geosci. Remote Sens.* 48, 1009–1018. <https://doi.org/10.1109/TGRS.2009.2030322>

GHRSSST Science Team, 2010. The recommended GHRSSST data specification (GDS) 2.0, document revision 5. Available from the GHRSSST International Project Office, 2011, pp. 123.

Gille, S.T., 2008. Decadal-Scale Temperature Trends in the Southern Hemisphere Ocean. *J. Clim.* 21, 4749–4765. <https://doi.org/10.1175/2008JCLI2131.1>

Good, S.A., Martin, M.J., Rayner, N.A., 2013. EN4: Quality controlled ocean temperature and salinity profiles and monthly objective analyses with uncertainty estimates. *J. Geophys. Res. Ocean.* 118, 6704–6716. <https://doi.org/10.1002/2013JC009067>

Guan, L., Kawamura, H., 2003. SST Availabilities of Satellite Infrared and Microwave Measurements. *J. Oceanogr.* 59, 201–209.

Høyer, J.L., Karagali, I., Dybkjær, G., Tonboe, R., 2012. Multi sensor validation and error characteristics of Arctic satellite sea surface temperature observations. *Remote Sens. Environ.* 121, 335–346. <https://doi.org/10.1016/j.rse.2012.01.013>

International Telecommunication Union, 2012. The Radio Regulations, 2012 ed. Geneva, Switzerland. [Available at http://en.wikipedia.org/wiki/ITU_Radio_Regulations].

Ishizaki, S., 2014. The State of the Western North Pacific in the First Half of 2013. *PICES Press* 22, 40.

Jones, M.S., Saunders, M.A., Guymer, T.H., 1996. Reducing cloud contamination in ATSR averaged sea surface temperature data. *J. Atmos. Ocean. Technol.* 13, 492–506.

Kilic, L., Prigent, C., Aires, F., Boutin, J., Heygster, G., Tonboe, R. T., & Donlon, C. (2018). Expected Performances of the Copernicus Imaging Microwave Radiometer (CIMR) for an All-Weather and High Spatial Resolution Estimation of Ocean and Sea Ice Parameters. *Journal of Geophysical Research: Oceans*, 123(10), 7564-7580.

Kennedy, J.J., 2014. A review of uncertainty in in situ measurements and data sets of sea surface temperature: In situ SST uncertainty. *Rev. Geophys.* 52, 1–32. <https://doi.org/10.1002/2013RG000434>

Le Traon, P.Y., Antoine, D., Bentamy, A., Bonekamp, H., Breivik, L.A., Chapron, B., Corlett, G., Dibarboure, G., Digiacomio, P., Donlon, C.J., Faugère, Y., Font, J., Girard-Ardhuin, F.,

Gohin, F., Johannessen, J.A., Kamachi, M., Lagerloef, G., Lambin, J., Larnicol, G., Le Borgne, P., Leuliette, E., Lindstrom, E., Martin, M.J., Maturi, E., Miller, L., Mingsen, L., Morrow, R., Reul, N., Rio, M.H., Roquet, H., Santoleri, R., Wilkin, J., 2015. Use of satellite observations for operational oceanography: recent achievements and future prospects. *J. Oper. Oceanogr.* 8, 12–27. <https://doi.org/10.1080/1755876X.2015.1022050>

Liang, X., Yang, Q., Nerger, L., Losa, S.N., Zhao, B., Zheng, F., Zhang, L., Wu, L., 2017. Assimilating Copernicus SST Data into a Pan-Arctic Ice-Ocean Coupled Model with a Local SEIK Filter. *J. Atmos. Ocean. Technol.* 34, 1985–1999. <https://doi.org/10.1175/JTECH-D-16-0166.1>

Maeda, T., Taniguchi, Y., Imaoka, K., 2016. GCOM-W1 AMSR2 Level 1R Product: Dataset of Brightness Temperature Modified Using the Antenna Pattern Matching Technique. *IEEE Trans. Geosci. Remote Sens.* 54, 770–782. <https://doi.org/10.1109/TGRS.2015.2465170>

Meissner, T., Wentz, F.J., 2012. The Emissivity of the Ocean Surface Between 6 and 90 GHz Over a Large Range of Wind Speeds and Earth Incidence Angles. *IEEE Trans. Geosci. Remote Sens.* 50, 3004–3026. <https://doi.org/10.1109/TGRS.2011.2179662>

Merchant, C. J., Harris, A. R., Roquet, H. and Le Borgne, P. (2009) Retrieval characteristics of non-linear sea surface temperature from the Advanced Very High Resolution Radiometer. *Geophysical Research Letters*, 36 (17). L17604. ISSN 0094-8276 doi: <https://doi.org/10.1029/2009GL039843>

Merchant, C.J., Embury, O., Rayner, N.A., Berry, D.I., Corlett, G.K., Lean, K., Veal, K.L., Kent, E.C., Llewellyn-Jones, D.T., Remedios, J.J., Saunders, R., 2012. A 20 year independent record of sea surface temperature for climate from Along-Track Scanning Radiometers. *J. Geophys. Res. Ocean.* 117. <https://doi.org/10.1029/2012JC008400>

Merchant, C.J., Embury, O., Roberts-Jones, J., Fiedler, E., Bulgin, C.E., Corlett, G.K., Good, S., McLaren, A., Rayner, N., Morak-Bozzo, S., Donlon, C., 2014. Sea surface temperature datasets for climate applications from Phase 1 of the European Space Agency Climate Change Initiative (SST CCI). *Geosci. Data J.* 1, 179–191. <https://doi.org/10.1002/gdj3.20>

Merchant, C.J., Le Borgne, P., 2004. Retrieval of sea surface temperature from space, based on modelling of infrared radiative transfer: Capabilities and limitations. *J. Atmos. Ocean. Technol.* 21, 1734–1746. <https://doi.org/10.1175/JTECH1667.1>

Merchant, C.J., Le Borgne, P., Marsouin, A., Roquet, H., 2008. Optimal estimation of sea surface temperature from split-window observations. *Remote Sens. Environ.* 112, 2469–2484. <https://doi.org/10.1016/j.rse.2007.11.011>

Monzikova, A.K., Kudryavtsev, V.N., Reul, N., Chapron, B., 2017. On the upper ocean response to tropical cyclones: Satellite microwave observation, in: *Progress in Electromagnetics Research Symposium-Fall (PIERS-FALL)*. IEEE, pp. 2437–2444. <https://doi.org/10.1109/PIERS-FALL.2017.8293545>

Nielsen-Englyst, P., Høyer, J.L., Pedersen, L.T., Gentemann, C.L., Alerskans, E., Block, T., Donlon, C., 2018. Optimal estimation of sea surface temperature from AMSR-E. *Remote Sens.* 10. <https://doi.org/10.3390/rs10020229>

Ning, J., Qing, X., Wang, T., Zhang, S., 2018. Upper Ocean Response to Super Typhoon Soudelor Revealed By Different SST Products, in: *IGARSS 2018-2018 IEEE International Geoscience and Remote Sensing Symposium*. IEEE. <https://doi.org/10.1109/IGARSS.2018.8518074>

O'Carroll, A.G., Eyre, J.R., Saunders, R.W., 2008. Three-way error analysis between AATSR, AMSR-E, and in situ sea surface temperature observations. *J. Atmos. Ocean. Technol.* 25, 1197–1207. <https://doi.org/10.1175/2007JTECHO542.1>

Rayner, N., Good, S., Block, T., 2015. SST CCI Product User Guide, Project Document, SST_CCI-PUG-UKMO-201. <http://www.esa-sst-cci.org/PUG/documents.htm>.

Reynolds, R.W., Rayner, N.A., Smith, T.M., Stokes, D.C., Wang, W., 2002. An improved in situ and satellite SST analysis for climate. *J. Clim.* 15, 1609–1625.

Roemmich, D., Johnson, G.C., Riser, S., Davis, R., Gilson, J., Owens, W.B., Garzoli, S.L., Schmid, C., Ignaszewski, M., 2009. The Argo Program: Observing the Global Ocean with Profiling Floats. *Oceanography* 22, 34–43. <https://doi.org/10.5670/oceanog.2009.36>

Rossow, W.B., 1993. Clouds, in: Gurney, R.J., Foster, J.L., Parkinson, L. (Eds.), *Atlas of Satellite Observations Related to Global Change*. Cambridge University Press, pp. 141–163.

Shibata, A., 2006. Features of ocean microwave emission changed by wind at 6 GHz. *J. Oceanogr.* 62, 321–330. <https://doi.org/10.1007/s10872-006-0057-3>

Udaya Bhaskar, T.V.S., Rahman, S.H., Pavan, I.D., Ravichandran, M., Nayak, S., 2009. Comparison of AMSR-E and TMI sea surface temperature with Argo near-surface temperature over the Indian Ocean. *Int. J. Remote Sens.* 30, 2669–2684. <https://doi.org/10.1080/01431160802555796>

Vásquez-Cuervo, J., Armstrong, E.M., Harris, A., 2004. The effect of aerosols and clouds on the retrieval of infrared sea surface temperatures. *J. Clim.* 17, 3921–3933. [https://doi.org/10.1175/1520-0442\(2004\)017<3921:TEOAAAC>2.0.CO;2](https://doi.org/10.1175/1520-0442(2004)017<3921:TEOAAAC>2.0.CO;2)

Wentz, F.J., Meissner, T., 2007. Supplement 1 Algorithm Theoretical Basis Document for AMSR-E Ocean Algorithms, RSS Technical Report 051707. Remote Sensing Systems, Santa Rosa, CA.

Wentz, F.J., Meissner, T., 2000. Algorithm Theoretical Basis Document (ATBD): AMSR Ocean Algorithm (Version 2), RSS Tech. Proposal 121599A-1. Remote Sensing Systems, Santa Rosa, CA.

Woodruff, S.D., Worley, S.J., Lubker, S.J., Ji, Z., Eric Freeman, J., Berry, D.I., Brohan, P., Kent, E.C., Reynolds, R.W., Smith, S.R., Wilkinson, C., 2011. ICOADS Release 2.5: extensions and enhancements to the surface marine meteorological archive. *Int. Journal Climatol.* 31, 951–967. <https://doi.org/10.1002/joc.2103>

Yang, C.-S., Kim, S.-H., Ouchi, K., Back, J.-H., 2015. Generation of high resolution sea surface temperature using multi-satellite data for operational oceanography. *Acta Oceanol. Sin.* 34, 74–88. <https://doi.org/10.1007/s13131-015-0694-8>

3. TECHNICAL CONSIDERATIONS FOR THE PMW RETRIEVAL IMPLEMENTATION

The approach used in this work package was to implement a DMI MW SST retrieval method in the UoR GBCS processing system used extensively elsewhere in the project. This effectively exploited the respective expertise available at the two institutions with DMI recoding their existing retrieval scheme as FORTRAN routines that interfaced with the GBCS system and UoR adapting the python framework and GBCS FORTRAN code to provide the data required for MW processing and to interpret and format the output consistently with the rest of the project. Initial work had taken place under WP23 in an experimental branch of the GBCS code to investigate the feasibility of MW retrievals using AMSR2 data. In this, individual AMSR2 data files could already be ingested and a radiative transfer model run but a full retrieval scheme had not been implemented. These changes were integrated into the main processing body of the code under this WP.

Initial file processing for AMSR-E was undertaken using a python script that made use of the hdf4cf utility to convert the original data files from HDF4 to netCDF format and then enforce CF-compliance. The netCDF files could then be read by one of the existing GBCS routines. AMSR2 hdf5 data files were ingested directly into the GBCS processor using the toolkit "AMTK" provided by JAXA. This toolkit required significant effort to integrate successfully with the modern FORTRAN 2003 code used in GBCS. Adaptations required by the code to use the data included intelligently handling the scanline based quality information rather than per pixel values, reformatting the time information, and converting the solar and view angles to standard definitions.

Changes were made to the staging of NWP data to make cloud liquid water available to the processor. Tie points for the intermediate meteorological files were set at every 4th pixel (~40 km). New configuration files were created to specify the characteristics of the MW instrument and the parameters required for the retrievals. Alterations were made to the existing retrieval interface and output structures to make the retrieved total column of water vapour and wind speed available in addition to the retrieved SST.

Adjustments were made to the way the diurnal variability model was applied to the retrieved data to eliminate a skin adjustment as MW instruments measure "sub-skin" SSTs rather than "skin" values.

4. IMPACT ASSESSMENT OF LEVEL 2 PMW CDR ON LEVEL 4 ANALYSIS

4.1 Introduction

The Operational Sea Surface Temperature and Sea Ice Analysis (OSTIA) system (Donlon, et al. 2012) is run operationally at the Met Office. It assimilates a variety of satellite retrieved SSTs and in situ observations to produce a daily, global SST analysis. The outputs are disseminated by the Copernicus Marine Environment Monitoring Service (CMEMS; marine.copernicus.eu) and are used for purposes such as for the boundary conditions for numerical weather predictions.

The OSTIA system has been configured to produce analyses for the ESA SST CCI project (Merchant, Embury, et al. 2014) (Merchant 2019). In this configuration, only satellite retrieved SSTs from the ATSR and AVHRR series of infra-red sensors are used to calculate the analysis in order to create the most stable dataset for climate researchers. The disadvantage to this choice is that there may be locations around the globe where there are persistently no inputted SSTs. This may occur, for example, due to cloud, which obscures the IR sensor's view of the surface. In the situation where there are no input data, the analyses relax towards climatology.

The climatology used in the system that generated the phase 2 SST CCI analyses was created from the phase 1 SST CCI analyses. Validation of these analyses has revealed that there are locations where they tended to be negatively biased such as in the north-west Indian Ocean (See PVIR report (Corlett, et al. 2014)). It was suspected that this was due to tropospheric aerosols. These biases will therefore also appear in the phase 2 analyses when there are no input data in those locations.

SSTs retrieved from PMW data have the potential to overcome these issues as they are able to provide data in some situations where IR-based SSTs are not available. To test this, some of the phase 2 SST CCI analyses were reprocessed with PMW CDR data assimilated in addition to the IR CDR data. By running the OSTIA system with the reprocessed PMW observations and comparing the output to a control IR dataset, we can determine their impact. The PMW observation datasets under investigation are from two instruments, AMSR-E (time range 200206 - 201109) and AMSR2 (201207 – 201612).

However, note that the PMW data are sparser than the IR data as they are subsampled to a 25 km spacing rather than 6 km spacing used for IR. This is because the viewing footprint of the PMW instruments is larger than for the IR instruments. Therefore, it is anticipated that the IR data will dominate outside of regions where the IR data are persistently missing.

In addition to comparing the SST analyses, comparisons are made of observation influence analyses (OIA) values produced by the OSTIA system. The SST analyses are produced by combining a first guess SST field (which is based on the previous day's SST analysis) with the satellite SSTs. The OIA values signify the relative weighting of the first guess field and the satellite SSTs in each grid location. A grid box with a value of 0 indicates that no observations were found for that pixel and that the first guess datum was used instead. Values of ~1 indicate that observations dominated in that grid box. By comparing the observation influence analysis (OIA) values from the analyses that used PMW data to the control which used only IR data, we can determine whether PMW observations are adding value to otherwise unobserved regions, and which areas of the planet see the greatest impact. Finally, statistics have been generated using near-surface Argo data as reference. Since Argo data is not used in the analyses, these provide an independent measure of whether the PMW data are improving or degrading the analyses.

4.2 Results

Figure 13 shows daily global averages of the OIAs. It can be seen that the PMW analyses have a consistently higher global average OIA than the control dataset. This indicates that the PMW data are having an impact on the analyses. Note that the zero values on the plot correspond to the gap between AMSR-E and AMSR2 observations.

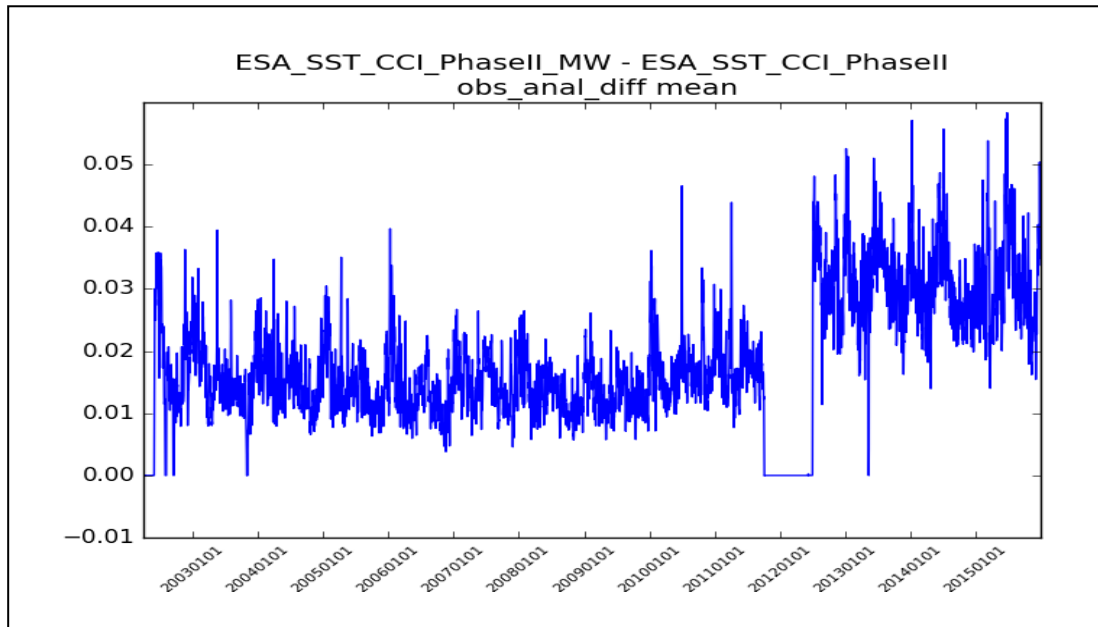


Figure 13: Difference in daily global OIA values.

In order to gain insight into the distribution of the differences in OA values, plots of the difference in the global monthly average OIA values were generated. Throughout the time period, it can be seen that the greatest increase in OA are observed in the tropical regions, especially in the coastal areas. Figure 14 displays examples from 2010 to illustrate the typical distribution in OA values.

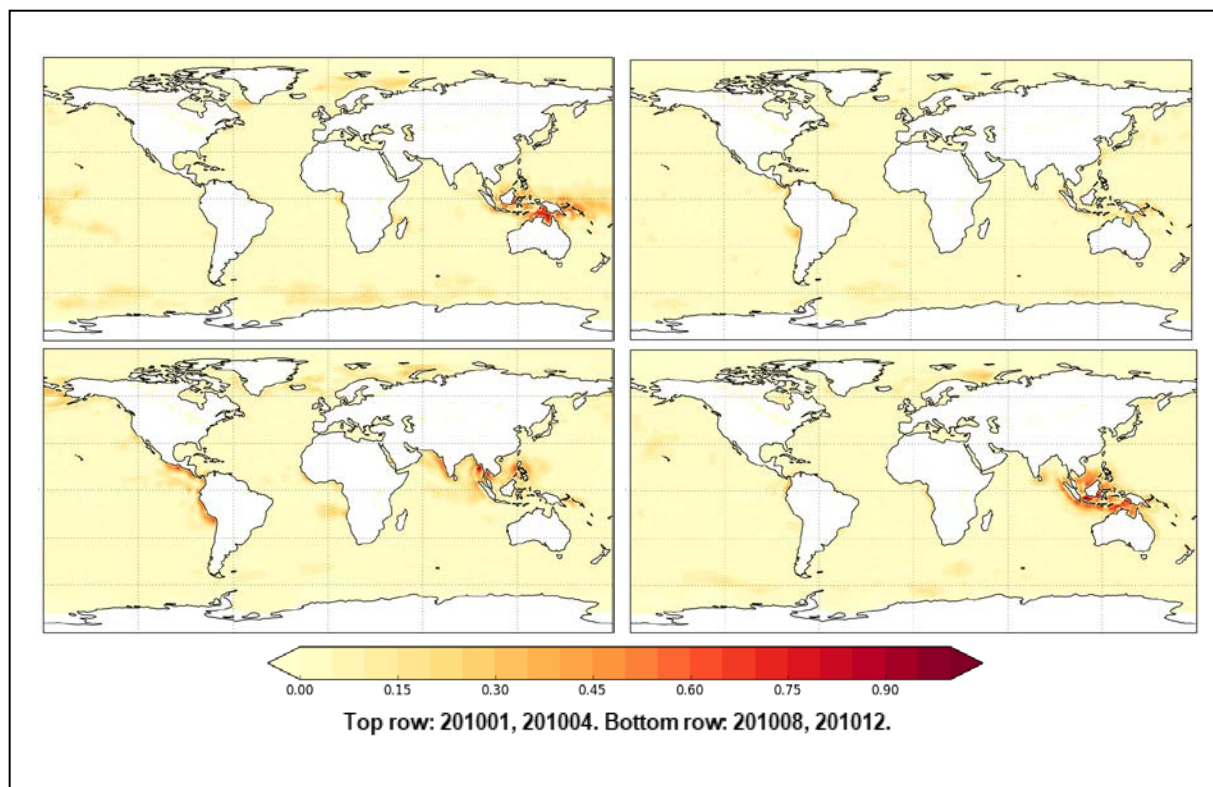


Figure 14: Global monthly average observation analysis values.

A comparison of SSTs reveals that the PMW analyses have slightly but consistently hotter global average daily SST values (Figure 15). This could be a result of the larger number of tropical observations correcting cold biases in the IR-only analyses. However, it could also be a symptom of a relative bias between the IR and PMW input data. Maps of the global monthly average SST differences (Figure 16) show that, although the analyses are warmer at the equator – there are also warm temperature patches observed in the North Pacific, even towards the Arctic regions. Interestingly – while the effect is apparent with AMSR-E data, the warm Arctic patches increase in intensity when using AMSR2 observations.

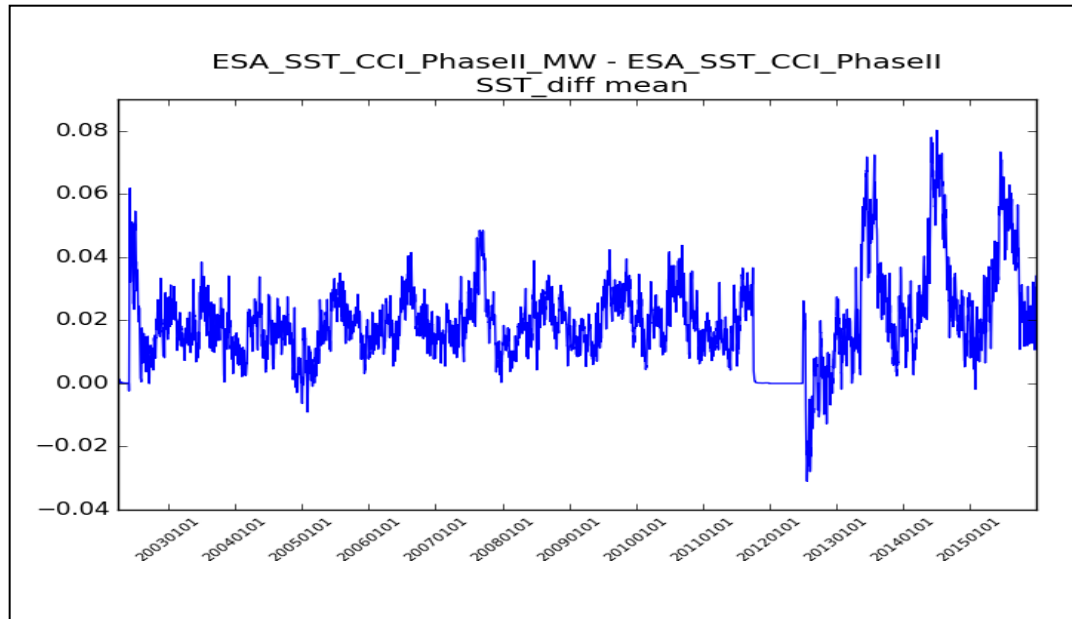


Figure 15: Difference in daily global average SST values

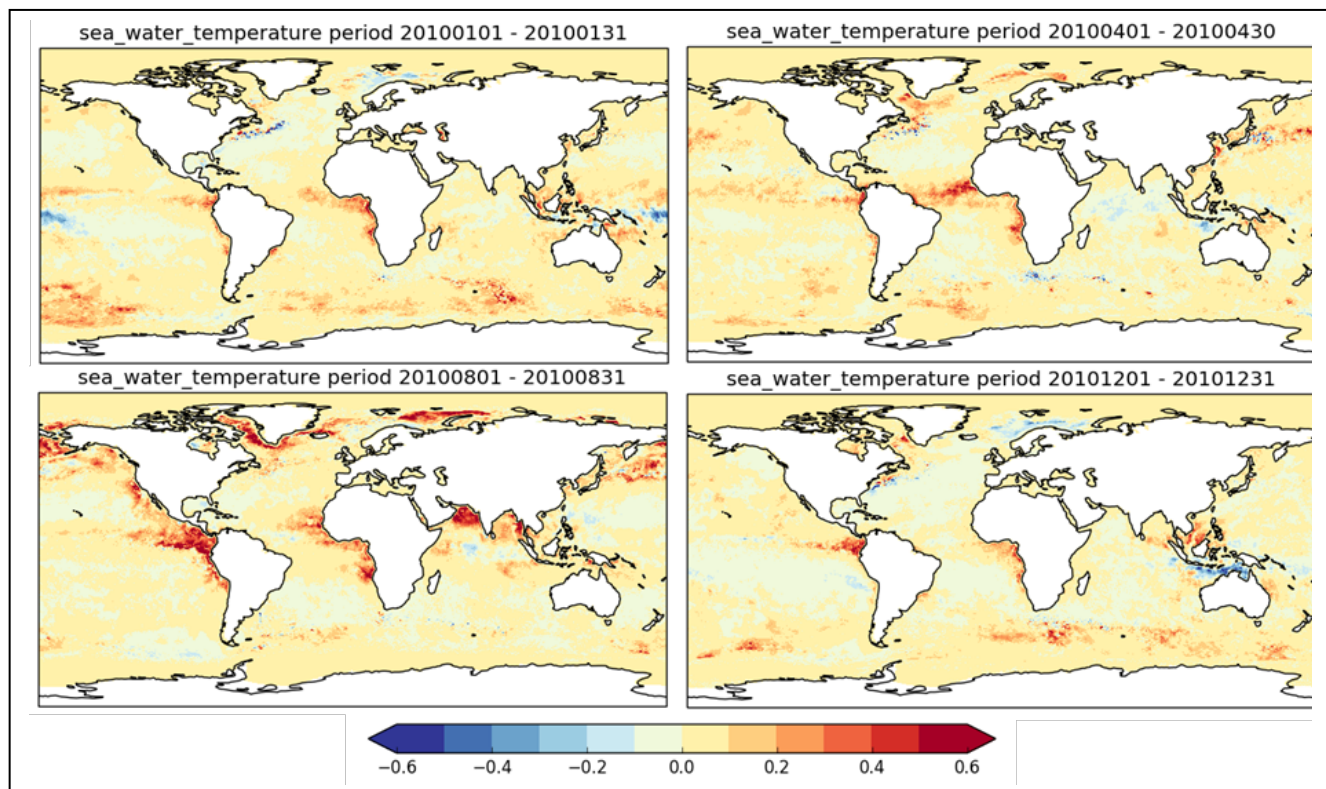


Figure 16: Global monthly SST difference

An examination of monthly maps of the difference in standard deviation of SST (Figure 17) shows that the inclusion of the PMW data is having an impact on SST variability. Most of the stronger differences in SD values occur in patches. However, it is not possible to determine from these whether the PMW data is improving the quality of the analysis.

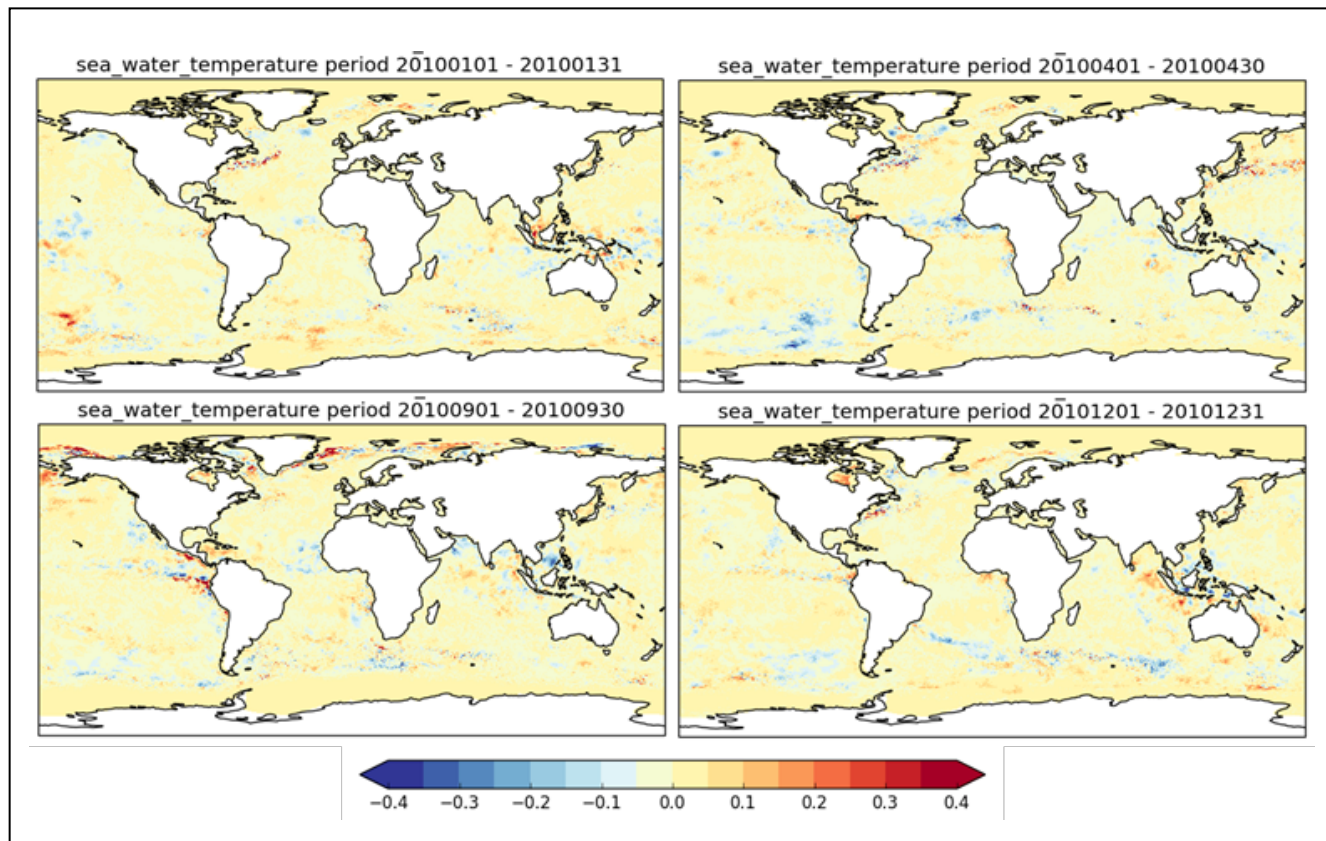


Figure 17: Global monthly SD difference

Argo near-surface observations have been compared to the two sets of analyses in order to determine if the PMW data are improving the analyses. The Argo data are high quality and independent since they are not used in the analyses, and have been used previously to assess SST CCI analyses (Fiedler, et al. 2019). The results for AMSR-E and AMSR2 are shown in Table 8 and Table 9 respectively.

As found previously, the PMW data have tended to warm the analyses and there is a reduced mean difference to Argo data in many regions. The standard deviation of differences has also been reduced broadly across the globe, which indicates a positive impact from the PMW data.

Table 8: Statistics of the differences between the analyses and Argo data for the AMSR-E period. Where statistics are better by at least 0.02 between the types of analysis, the better of the two is highlighted in bold

Region	IR – only analyses		IR and PMW analyses		
	Mean difference (K)	Standard deviation of differences (K)	Mean difference (K)	Standard deviation of differences (K)	Number of matchups
Globe	-0.065	0.445	-0.040	0.415	473987
Arctic	-0.188	0.532	-0.149	0.488	2754
Mediterranean Sea	0.093	0.762	0.101	0.761	2941
North Atlantic	-0.056	0.549	-0.027	0.517	63605
Tropical Atlantic	-0.110	0.359	-0.053	0.324	24402
South Atlantic	-0.056	0.432	-0.038	0.406	39860
North Pacific	-0.059	0.478	-0.022	0.444	166408
Tropical Pacific	-0.062	0.278	-0.042	0.260	102518
South Pacific	-0.064	0.342	-0.052	0.325	113292
Indian Ocean	-0.084	0.392	-0.060	0.352	84471
Southern Ocean	-0.087	0.446	-0.066	0.423	93927

Table 9: Statistics of the differences between the analyses and Argo data for the AMSR2 period. Where statistics are better by at least 0.02 between the types of analysis, the better of the two is highlighted in bold

Region	IR – only analyses		IR and PMW analyses		Number of matchups
	Mean difference (K)	Standard deviation of differences (K)	Mean difference (K)	Standard deviation of differences (K)	
Globe	0.053	0.452	0.026	0.395	337634
Arctic	0.065	0.552	-0.048	0.526	3040
Mediterranean Sea	-0.036	0.440	-0.042	0.433	6831
North Atlantic	0.069	0.477	0.038	0.414	59418
Tropical Atlantic	0.186	0.386	0.084	0.316	25910
South Atlantic	0.072	0.540	0.033	0.468	25840
North Pacific	0.036	0.468	0.002	0.410	116885
Tropical Pacific	0.043	0.310	0.033	0.272	93485
South Pacific	0.044	0.368	0.035	0.326	86940
Indian Ocean	0.097	0.417	0.065	0.352	47506
Southern Ocean	0.070	0.525	0.037	0.459	63027

To examine the impact of PMW data on feature resolution, power spectra plots were generated for three regions:

1. Gulf Stream: (North Atlantic), 38.875-45.125 N, 65.125-49.875 W
2. Kuroshio: (North Pacific), 32.5-45.125 N, 141.875-170.125 E
3. Agulhas Retroflexion Current: (South Atlantic), 45-27 S, 9.875-50.125 E

Monthly and yearly plots were generated for each region over the whole period. The results show very little difference between the control and IR+PMW data. Plots from 2010 are included as an example (Figure 18). It seems that the benefits of PMW data are over larger domains than the three areas investigated. In addition, the biggest differences observed in the monthly mean and standard deviation SST plots (Figure 16 & Figure 17) were in the tropics and especially in the coastal areas (such as the Philippines) whereas the three domains explored here are in the higher/lower latitudes. Time constraints mean that we are unable to explore this avenue of investigation further.

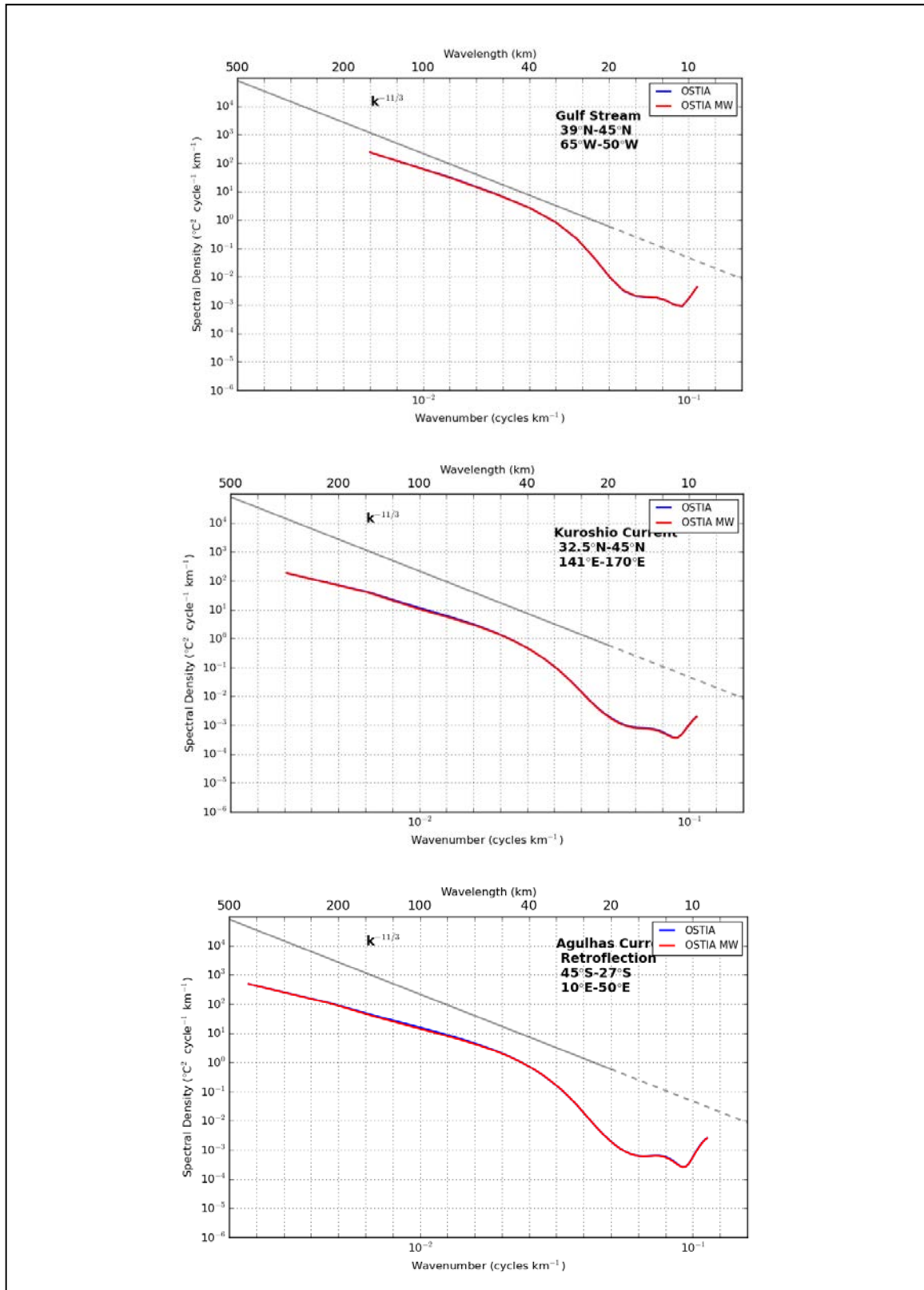


Figure 18: Regional power spectra plots.

4.3 Summary

Comparisons of analyses where only IR data are used to analyses where PMW and IR are combined show that PMW observations increase the number of observations in regions that are currently poorly observed in the IR dataset. However, the impact of the PMW data is not limited to those regions as demonstrated by maps of difference in SST and standard deviation of SST. This is perhaps surprising because the PMW data is relatively sparse compared to the IR data. On a global average, SSTs are warmed by the inclusion of PMW data. The PMW data's impact on SST standard deviation is variable and sometimes has the effect of increasing or decreasing the standard deviation, depending on location. Statistics of differences between the analyses and independent Argo data show a clear benefit from use of PMW data.

These results demonstrate that the inclusion of PMW data is beneficial to the analyses and that there is a strong case for including them in the next reprocessing of the CDR.

4.4 Bibliography

Corlett, Gary, Chris Atkinson, Nick Rayner, Simon Good, Emma Fiedler, Alison McLaren, Jacob Hoeyer, and Claire Bulgín. 2014. "CCI Phase 1 (SST) Product Validation and Intercomparison Report (PVIR)."

Donlon, Craig, Matthew Martin, John Stark, Jonah Roberts-Jones, Emma Fiedler, and Werenfrid Wimmer. 2012. "The Operational Sea Surface Temperature and Sea Ice Analysis (OSTIA) system." *Remote Sensing of Environment* 116: 140-158. doi:<https://doi.org/10.1016/j.rse.2010.10.017>.

Fiedler, Emma, Alison McLaren, Viva Banzon, Bruce Brasnett, Shiro Ishizaki, John Kennedy, Nick Rayner, et al. 2019. "Intercomparison of long-term sea surface temperature analyses using the GHRSSST Multi-Product Ensemble (GMPE) system." *Remote Sensing of Environment* 222: 18-33. doi:<https://doi.org/10.1016/j.rse.2018.12.015>.

Merchant, Christopher. 2019. "(In Prep) Sea surface temperature datasets for climate applications from Phase 2 of the European Space Agency Climate Change Initiative (SST CCI)."

Merchant, Christopher, Owen Embury, Jonah Roberts-Jones, Emma Fiedler, Claire Bulgín, Gary Corlett, Simon Good, et al. 2014. "Sea surface temperature datasets for climate applications from Phase 1 of the European Space Agency Climate Change Initiative (SST CCI)." *Geoscience Data Journal* 179-191. doi:<https://doi.org/10.1002/gdj3.20>.

5. CONCLUSIONS AND WAY FORWARD

The work presented in this report demonstrates that PMW satellite observations provide valuable observations to be used for monitoring the SST in non precipitating conditions. The funding for future microwave satellite missions is currently unsecure. A High Priority Candidate Mission (HPCM) called the Copernicus Imaging Microwave Radiometer is now being studied at the European Space Agency. The CIMR proposes a conically scanning radiometer with a swath > 1900 km. It will include channels at 1.4 GHz 6.9 and 10.65 GHz 18.8 GHz and 36.5 GHz on the same platform in a high inclination dawn-Dusk orbit coordinated with the MetOp-SG(B). The expected spatial resolution on the 6.9 GHz channel will be 15 km. The L2P retrieval algorithms presented here can easily be adapted to the CIMR frequencies taking into account the enhanced spatial resolution, improved NEdT and addition of an L-band channel. Based upon the results obtained here, it is therefore recommended that the CIMR satellite will be selected for an operational mission, to extend and improve on future PMW based SST CDRs.